

Valley-Polarized Quantum Anomalous Hall State in Moiré MoTe₂/WSe₂ Heterobilayers

Ying-Ming Xie¹, Cheng-Ping Zhang¹, Jin-Xin Hu¹, Kin Fai Mak^{2,3,4}, and K. T. Law^{1*}

¹*Department of Physics, Hong Kong University of Science and Technology, Clear Water Bay, Hong Kong, China*

²*School of Applied and Engineering Physics, Cornell University, Ithaca, NY, USA*

³*Kavli Institute at Cornell for Nanoscale Science, Ithaca, NY, USA and*

⁴*Laboratory of Atomic and Solid State Physics, Cornell University, Ithaca, NY, USA*

(Dated: January 17, 2022)

Moiré heterobilayer transition metal dichalcogenides (TMDs) emerge as an ideal system for simulating the single-band Hubbard model and interesting correlated phases have been observed in these systems. Nevertheless, the moiré bands in heterobilayer TMDs were believed to be topologically trivial. Recently, it was reported that both a quantum valley Hall insulating state at filling $\nu = 2$ (two holes per moiré unit cell) and a valley-polarized quantum anomalous Hall state at filling $\nu = 1$ were observed in AB stacked moiré MoTe₂/WSe₂ heterobilayers. However, how the topologically nontrivial states emerge is not known. In this work, we propose that the pseudo-magnetic fields induced by lattice relaxation in moiré MoTe₂/WSe₂ heterobilayers could naturally give rise to moiré bands with finite Chern numbers. We show that a time-reversal invariant quantum valley Hall insulator is formed at full-filling $\nu = 2$, when two moiré bands with opposite Chern numbers are filled. At half-filling $\nu = 1$, Coulomb interaction lifts the valley degeneracy and results in a valley-polarized quantum anomalous Hall state, as observed in the experiment. Our theory identifies a new way to achieve topologically non-trivial states in heterobilayer TMD materials.

Introduction.— Recently, there is an intense study on the moiré superlattices such as in twisted bilayer graphene [1–10] and twisted bilayer transition metal dichalcogenides (TMDs) [11–29]. The narrow moiré bands together with strong electron-electron interactions give rise to various interesting quantum states of matter.

The moiré superlattices formed by TMD heterobilayers are particularly interesting [16–30]. A moiré TMD heterobilayer is formed by stacking two different 2H-structure monolayer TMDs MX₂ and M'X₂. Due to the large energy offset of the valence bands of the two TMDs, the electrons near the Fermi energy are mostly originated from the TMD layer with higher valence band energy. Therefore, a moiré TMD heterobilayer can be approximately treated as a monolayer TMD with an additional moiré potential which is created through interlayer couplings. Moreover, due to the large Ising spin-orbit coupling [31–33], spin degeneracy is lifted while the valley degeneracy plays the role of pseudo-spin. In the presence of Coulomb interactions, a moiré TMD heterobilayer can be treated as a single-band Hubbard model simulator [18, 23] with parameters highly tunable through the twist angle and the displacement field. Several interesting correlated phenomena such as Mott insulating states[23], Wigner crystal states[24], Pomeranchuk effect and continuous Mott transition [29] have been observed in AA stacked moiré TMD heterobilayers. However, so far the moiré bands in heterobilayers are expected to be topologically trivial and topology does not play a role in these correlated phases.

Surprisingly, in a recent experiment with AB stacked

moiré MoTe₂/WSe₂ heterobilayers, a quantum valley Hall insulator state at full-filling $\nu = 2$, i.e., two holes per moiré unit cell, and a quantum anomalous Hall state at half-filling $\nu = 1$ were observed [34]. As the quantized Hall resistance strongly correlates with valley polarization through magnetic circular dichroism measurements, it is strongly suggestive that the quantum anomalous Hall state is a valley-polarized anomalous Hall state[34]. Although it was predicted that the quantum valley Hall state can emerge in homobilayer TMDs [14] which can be described by a Kane-Mele model [35], the low energy description of heterobilayers is dramatically different due to the large offset of the energy of the bands which is estimated to be around 300 meV [29, 34] and large differences in interlayer tunnelling strength. Therefore, the origin of the topologically non-trivial bands in heterobilayers is not known.

In this work, we point out that a periodically modulated pseudo-magnetic field, which could emerge spontaneously under lattice relaxation, can give rise to topologically nontrivial moiré bands. Specifically, (i) the pseudo-magnetic field can create Chern bands with opposite Chern numbers at opposite valleys. As a result, a quantum valley Hall insulating phase would form at $\nu = 2$, when the topmost moiré bands at two valleys are filled; (ii) Importantly, at half-filling $\nu = 1$, based on a self-consistent Hartree-Fock calculation, we found the Coulomb interactions could lift the degeneracies of the two valleys. It results in an interactions-driven valley-polarized quantum anomalous Hall phase as observed in the recent experiments. Our theory identifies a new way to achieve topologically non-trivial states in heterobilayer TMD materials which were considered topologically trivial.

Model.— As pointed out in Ref. [18], due to the

*Corresponding author.
phlaw@ust.hk

large Ising spin-orbit coupling which breaks the spin-degeneracy and the layer asymmetry, a TMD heterobilayer can be described by a single-band Hubbard model with the valley degrees of freedom playing the role of pseudo-spins. However, the resulting moiré bands are topologically trivial. One important element which was not considered in the original model of TMD heterobilayer [18] is lattice relaxation. Indeed, it has been shown that local strain can result in lattice relaxation and even lattice reconstructions which are important in twisted bilayer graphene [36, 37] and twisted TMDs [38–43]. Importantly, the lattice relaxation can generate periodically modulated pseudo-magnetic fields which play an important role in the moiré band structure [36].

To capture the effects of periodic pseudo-magnetic fields $B(\mathbf{r})$, we include an additional gauge field \mathbf{A} with $B(\mathbf{r}) = \nabla \times \mathbf{A}(\mathbf{r})$ into the previously proposed model Hamiltonian for the moiré TMD heterobilayer [18, 27] as $H = \int d\mathbf{r} \psi_\tau^\dagger(\mathbf{r}) \mathcal{H}_\tau(\mathbf{r}) \psi_\tau(\mathbf{r})$. Here,

$$\mathcal{H}_\tau(\mathbf{r}) = -\frac{(\hat{\mathbf{p}} + \tau e \mathbf{A})^2}{2m^*} + V(\mathbf{r}), \quad (1)$$

where the momentum operator $\hat{\mathbf{p}} = -i\hbar\nabla$, m^* is the valence band effective mass, $\tau = \pm$ for $\pm K$ valley. The moiré potential is $V(\mathbf{r}) = 2V_0 \sum_{j=1,3,5} \cos(\mathbf{G}_j \cdot \mathbf{r} + \phi)$ with moiré wave vectors $\mathbf{G}_j = \frac{4\pi}{\sqrt{3}L_M} (\cos(\frac{(j-1)\pi}{3}), \sin(\frac{(j-1)\pi}{3}))$, $L_M \approx a/\sqrt{\delta^2 + \theta^2}$ is the moiré lattice constant with a lattice constant mismatch $\delta = (a - a')/a$ and a twist angle θ . To be specific, we adopted the parameters: $m^* = 0.6m_0$ with m_0 the electron mass, $a = 3.565\text{\AA}$, $a' = 3.317\text{\AA}$ [44–46] for the band structure calculations of TMD MoTe₂/WSe₂ heterobilayers, where the top valence moiré bands originate from MoTe₂ layer [29, 34]. The model Hamiltonian H respects C_3 symmetry and time-reversal symmetry $T = \tau_x \hat{K}$ with \hat{K} as complex conjugate operation, and the moiré Hamiltonians of the two valleys are related by time-reversal symmetry: $T\mathcal{H}_\tau(\mathbf{r})T^{-1} = \mathcal{H}_{-\tau}(\mathbf{r})$.

We first consider the case without the pseudo-magnetic fields $B(\mathbf{r})$, i.e., $\mathbf{A} = 0$, the moiré Hamiltonian exhibits a spinless time-reversal symmetry: $T'\mathcal{H}_\tau(\mathbf{r})T'^{-1} = \mathcal{H}_\tau(\mathbf{r})$ with $T' = \hat{K}$. This spinless time-reversal symmetry enforces the Berry curvature to be an odd function: $\Omega(\mathbf{k}) = -\Omega(-\mathbf{k})$ (Supplementary Material (SM) Sec. I[47]). As a result, the Chern number of each moiré band is zero. To break this spinless time-reversal symmetry, an additional periodically modulated pseudo-magnetic field \mathbf{B} is introduced in the moiré Hamiltonian (1). Evidently, in this case $T'\mathcal{H}_\tau(\mathbf{r})T'^{-1} \neq \mathcal{H}_\tau(\mathbf{r})$. Hence, moiré bands with finite Chern numbers are allowed.

To be specific, we consider a C_3 -invariant periodic pseudo-magnetic field: $B(\mathbf{r}) = B_0 \sum_{j=1,3,5} \cos(\mathbf{G}_j \cdot \mathbf{r})$, which is expected to emerge in an AB stacked moiré TMD bilayer under lattice relaxation as shown in Ref. [38] or can be generated by some out of plane corrugation effects [48, 49]. The topography of this pseudo-magnetic field is shown in Fig. 1(a). It displays the same period as the

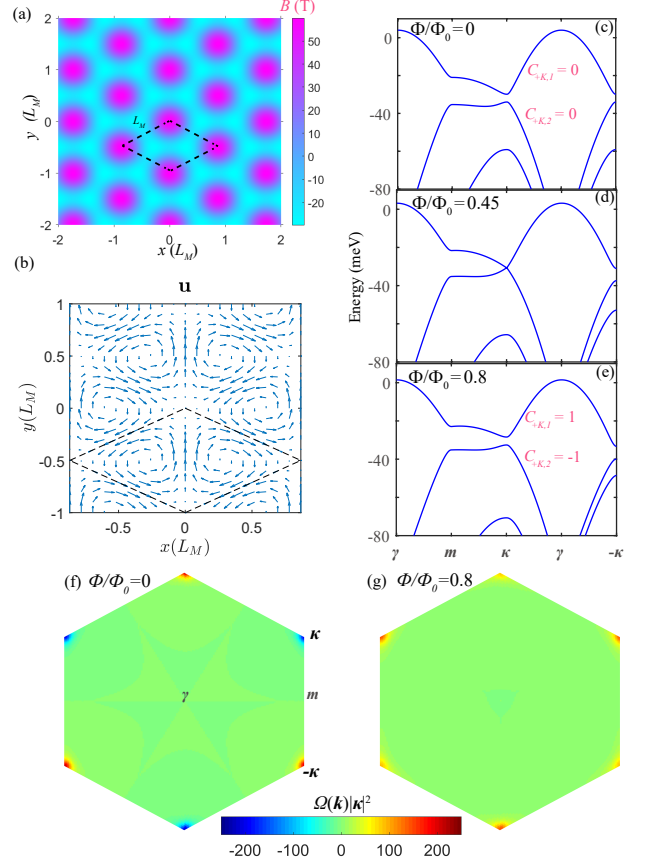


FIG. 1: (a) and (b) show the topography of a C_3 symmetric periodic pseudo-magnetic field ($B_0 = 20\text{T}$) and the corresponding strain displacement field \mathbf{u} , respectively. (c), (d) and (e) show the moiré band structures at valley K calculated at $\Phi/\Phi_0 = 0, 0.45, 0.8$ respectively, where the moiré potential parameters are taken as $V_0 = 10\text{ meV}$, $\phi = 0.3\pi$, $\theta = 0.53^\circ$. The top two moiré bands at Φ/Φ_0 with Chern number $C_{K,1}$ and $C_{K,2}$ are highlighted. The corresponding distributions of the Berry curvature within moiré Brillouin zone at $\Phi/\Phi_0 = 0$ and $\Phi/\Phi_0 = 0.8$ are shown in (f) and (g), respectively.

moiré superlattice, and it is important to note that the net flux in each moiré unit cell is zero, as we will see later the topology of this system can be understood in terms of the Haldane model [50]. The corresponding gauge field of $B(\mathbf{r})$ is derived as $\mathbf{A}(\mathbf{r}) = A_0[\mathbf{a}_2 \sin(\mathbf{G}_1 \cdot \mathbf{r}) - \mathbf{a}_1 \sin(\mathbf{G}_3 \cdot \mathbf{r}) - \mathbf{a}_3 \sin(\mathbf{G}_5 \cdot \mathbf{r})]$, where $\mathbf{a}_1 = (\frac{\sqrt{3}}{2}, \frac{1}{2})L_M$, $\mathbf{a}_2 = (0, 1)L_M$, $\mathbf{a}_3 = \mathbf{a}_2 - \mathbf{a}_1$, and $A_0 = \sqrt{3}B_0/4\pi$. This gauge field can be generated by a two-dimensional strain field $u_{ij}(\mathbf{r}) = (\partial_i u_j(\mathbf{r}) + \partial_j u_i(\mathbf{r}))/2$ [48, 51, 52] with $\mathbf{A} = \alpha(2u_{xy}, u_{xx} - u_{yy})$. The strain displacement field that gives rise to the periodic $B(\mathbf{r})$ is plotted in Fig. 1(b) (see the detail in Supplementary Material (SM)[47]). The periodic strain displacement has been observed in moiré TMD bilayers [41–43]. Physically, there are different types of local stacking configurations which result in different lattice relaxation within a moiré unit cell [38, 47].

As presented in SM [47] such lattice relaxation could generate the periodic pseudomagnetic fields we introduced.

Inserting $\mathbf{A}(\mathbf{r})$ into Eq. (1), we obtained $\mathcal{H}_\tau(\mathbf{r}) = -\frac{(\hat{\mathbf{p}} + \tau \frac{\Phi_0}{2m^*} \tilde{\mathbf{A}})^2}{2m^*} + V(\mathbf{r})$, where $\Phi_0 = \frac{h}{e}$ is a flux quantum and $\tilde{\mathbf{A}} = \frac{\sqrt{3}}{2} B_0 L_M^2 \hat{\mathbf{e}}_z$ has the dimension of magnetic flux, $\tilde{\mathbf{A}} = \frac{4\pi \mathbf{A}(\mathbf{r})}{\sqrt{3} B_0 L_M^2}$. We can then diagonalize $\mathcal{H}_\tau(\mathbf{r})$ with plane wave basis to obtain the moiré bands (SM Sec. IVA [47]).

As an illustration, in Fig. 1(c) to (e), we show the energy spectrum of $+K$ valley ($\tau = +1$) at a commensurate angle $\theta = 0.53^\circ$ [27] but with different strength of pseudo-magnetic field: $\Phi/\Phi_0 = 0, 0.45, 0.8$. The corresponding Berry curvature distribution of top moiré bands at $\Phi/\Phi_0 = 0$ and $\Phi/\Phi_0 = 0.8$ are shown in Fig. 1(f) and Fig. 1(g). Without the pseudo-magnetic field, the moiré band carries zero Chern number (labeled in Fig. 1(c)),

$$H_{\pm\kappa}^{eff}(\mathbf{k}) = \begin{pmatrix} \epsilon_0 + 2V_0 \cos \phi & \pm \frac{1}{2}v(k_x + ik_y) & \pm \frac{1}{2}v(k_x - ik_y) \\ \pm \frac{1}{2}v(k_x - ik_y) & \epsilon_0 + 2V_0 \cos(\frac{2\pi}{3} + \phi) \mp \epsilon_B & \pm \frac{1}{2}v(k_x + ik_y) \\ \pm \frac{1}{2}v(k_x + ik_y) & \mp \frac{1}{2}v(k_x - ik_y) & \epsilon_0 + 2V_0 \cos(\frac{4\pi}{3} + \phi) \pm \epsilon_B \end{pmatrix}, \quad (2)$$

where \mathbf{k} is expanded near $\pm\kappa$, $\epsilon_0 = -\kappa^2/2m^*$, $v = \kappa/m^*$, $\epsilon_B = \frac{\sqrt{3}v}{4L_M} \frac{\Phi}{\Phi_0} = \frac{\hbar e B_0}{4m^*}$ is a magnetic energy due to the presence of pseudo-magnetic fields. Interestingly, this three-band Hamiltonian exhibits as a Dirac Hamiltonian at every two-band subspace. Moreover, the ϵ_B shifts the Dirac mass in opposite way at $+\kappa$ and $-\kappa$. This feature maps the effective Hamiltonian back to the Haldane model [50] and moiré bands with finite Chern number would thus be created when the Dirac mass term changes sign at $+\kappa$ or $-\kappa$. The topological phase transition boundary lines are obtained as:

$$L_1 : \frac{\epsilon_B}{V_0} = \pm 2[\cos(\frac{2\pi}{3} + \phi) - \cos \phi]; \quad (3)$$

$$L_2 : \frac{\epsilon_B}{V_0} = \pm 2[\cos \phi - \cos(\frac{4\pi}{3} + \phi)]; \quad (4)$$

$$L_3 : \frac{\epsilon_B}{V_0} = \pm [\cos(\frac{2\pi}{3} + \phi) - \cos(\frac{4\pi}{3} + \phi)]. \quad (5)$$

Surprisingly, the topological phase transition boundary lines L_j only rely on the ratio $\frac{\epsilon_B}{V_0}$ and the phase ϕ of the moiré potential in the perturbative regime, where the moiré bandwidth ϵ_W is much larger than the magnetic energy ϵ_B .

To determine the possible nontrivial topological regions, the Chern number C of the top moiré band with various ϕ and ratio ϵ_B/V_0 is calculated numerically (SM Sec. IVB [47]). The typical topological phase diagram within ($V_0 = 1$ meV) and beyond ($V_0 = 10$ meV) the perturbation region are displayed in Fig. 2(a) and Fig. 2(b), respectively, where C is found to be able to take the value of 0, ± 1 and ± 2 . The phase boundaries given by

although there appears to be finite Berry curvature at moiré Brillouin zone corners $\pm\kappa$ (Fig. 1(f)). With an increase in the pseudo-magnetic field, it can be seen that the gap at κ is closed at $\Phi/\Phi_0 = 0.45$ and reopens when $\Phi/\Phi_0 > 0.45$, which results in finite Chern numbers for the top two moiré bands (labeled in Fig. 1(e)). It is clear from Fig. 1(g) that, for the band with a finite Chern number, the Berry curvature has the same sign in the whole Brillouin zone.

Topological phase diagram.—To understand the topological phase transition, we derived an effective Hamiltonian near $\pm\kappa$ by performing perturbation theory at three moiré Brillouin corners connected by the reciprocal lattice vectors for the moiré pattern (SM Sec. IIA [47]). The resulting effective Hamiltonian is

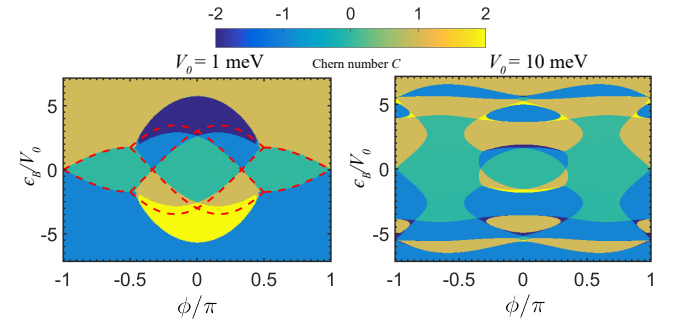


FIG. 2: (a) and (b) respectively, display the Chern number C as a function of phase ϕ and the strength of the pseudo-magnetic fields characterized by the ratio of ϵ_B/V_0 with $V_0 = 1$ meV and $V_0 = 10$ meV. The red dashed lines represent the phase boundaries given by the effective Hamiltonian.

the effective Hamiltonian (2) are also depicted in Fig. 2 as red dashed lines. In Fig. 2(a), impressively, most of the phase boundaries in numerical results match the results from the effective Hamiltonian. As shown in Fig. 2(b), the phase boundaries become more complicated beyond the perturbative regime. Nevertheless, there is still a large proportion of parameter space that exhibits Chern number $C = \pm 1$.

We now discuss the accessibility of parameter space with finite Chern numbers. As shown in Fig. 2, the optimal ϕ is near $\pi/3$ and π , and a large magnetic energy ϵ_B at the order of V_0 is desired. Note that the magnitude of $\epsilon_B = \frac{\hbar e B_0}{4m^*} \sim 0.05 B_0$ meV/T is determined by the strength of pseudo-magnetic fields B_0 . Considering a B_0

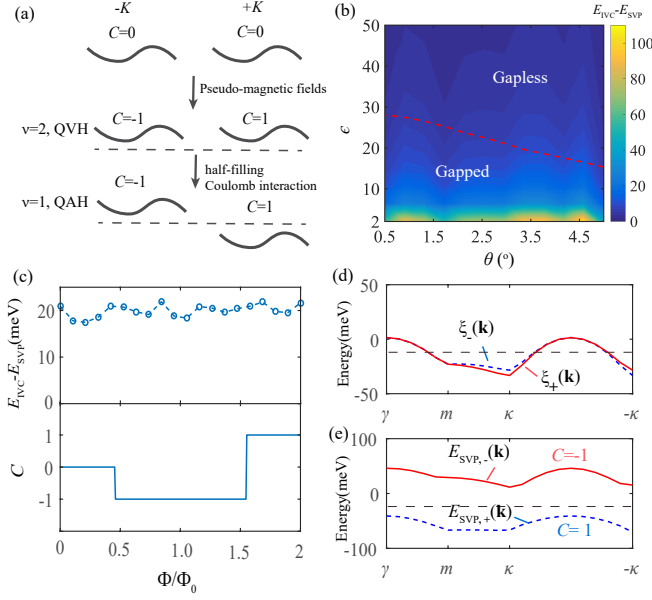


FIG. 3: (a) Schematic plot of the evolution of Chern number for top moiré bands at two valleys in the presence of pseudo-magnetic fields, different fillings and interaction with the emergence of quantum valley Hall (QVH) at filling $\nu = 2$ and valley-polarized quantum anomalous Hall (QAH) at filling $\nu = 1$. (b) The energy difference between the inter-valley coherent state (IVC) and the spin-valley-polarized (SVP) state: $E_{IVC} - E_{SVP}$ (in units of meV) as a function of dielectric constant ϵ and twist angle θ . (c) shows the evolution of $E_{IVC} - E_{SVP}$ (top panel) and Chern number (lower panel) at finite flux. (d) and (e), respectively, show the moiré band structures $\xi_{\tau}(\mathbf{k})$ and the mean-field band structures of the SVP state $E_{SVP,\tau}(\mathbf{k})$ at $\Phi/\Phi_0 = 0.8$. The parameters for moiré potential in (b) to (e) are taken as $V_0 = 10$ meV, $\phi = 0.3\pi$, $\theta = 0.53^\circ$. Here, $\epsilon = 10$, $\lambda^{-1} = 10$ nm [11, 29, 53] are adopted for (c) to (e).

of tens of T, the magnetic energy ϵ_B is estimated to be several meV which is achievable in heterobilayer TMDs and other moiré materials [38]. As shown in Fig. 2, this ϵ_B is certainly sufficient to drive the system to be topological for ϕ near $\pi/3$ and π , while for ϕ far from these regions, it would depend on the magnitude of V_0 . A large V_0 would tend to make the system trivial since it would enhance the trivial energy gap between moiré bands. In the case of a large V_0 (tens of meVs), the topological region may still be achievable through a displacement field [29], because the displacement field effectively tunes the interlayer tunneling so that V_0 could be effectively changed.

valley-polarized quantum anomalous Hall states at half-filling $\nu = 1$.—After demonstrating the formation of Chern bands in moiré TMD heterobilayers with periodic pseudo-magnetic fields, we now study the interaction induced topological phases, as schematically depicted in Fig. 3(a). We consider the case where the Chern number $C = \pm 1$ at the $\pm K$ valley. Due to the spin-valley locking, the moiré TMD heterobilayer is a quantum val-

ley Hall insulating phase at the full-filling $\nu = 2$ (see Fig. 3(a)). When the chemical potential is tuned to half-filling $\nu = 1$, as we will demonstrate later, the Coulomb interaction could lift the valley degeneracy and thus gives rise to a valley-polarized quantum anomalous Hall insulator.

In moiré TMD heterobilayer, due to the spin-valley locking, the Coulomb interaction is simply

$$H_{int} = \frac{1}{2S} \sum_{\mathbf{k}, \mathbf{k}', \mathbf{q}} V(\mathbf{q}) c_{\tau}^{\dagger}(\mathbf{k} + \mathbf{q}) c_{\tau'}^{\dagger}(\mathbf{k}' - \mathbf{q}) c_{\tau'}(\mathbf{k}') c_{\tau}(\mathbf{k}), \quad (6)$$

where S is the sample area, $V(\mathbf{q}) = \frac{e^2}{2\epsilon\epsilon_0\sqrt{q^2 + \lambda^{-2}}}$ is the screened Coulomb interaction with ϵ , ϵ_0 , λ^{-1} denoting the dielectric constant, vacuum permittivity and a screened length. In practice, the dielectric constant and screened length are determined by the surrounding hBN and metallic gates [54]. Within the Hartree-Fock mean-field analysis, we define the order parameter as $\langle \psi_G | c_{\tau}^{\dagger}(\mathbf{k}) c_{\tau'}(\mathbf{k}') | \psi_G \rangle = \Delta_{\tau\tau'}(\mathbf{k}) \delta_{\mathbf{k}, \mathbf{k}'}$, where $|\psi_G\rangle$ denotes the ground state. Unlike moiré superlattices of graphene [9, 53, 55–57], here due to the spin-valley locking, the possible gapped correlated ground states for moiré TMD heterobilayer can be simply grouped into two categories at half-filling: (i) the spin-valley-polarized (SVP) state $|\psi_G\rangle = \Pi_{|\mathbf{k}| < k_F} c_{\tau}^{\dagger}(\mathbf{k}) |0\rangle$, where only τ -valley is occupied; (ii) the spin-valley-locked intervalley coherent (IVC) state $|\psi_G\rangle = \Pi_{|\mathbf{k}| < k_F} [\sin \frac{\theta_{\mathbf{k}}}{2} e^{-i\frac{\varphi_{\mathbf{k}}}{2}} c_{+}^{\dagger}(\mathbf{k}) + \cos \frac{\theta_{\mathbf{k}}}{2} e^{i\frac{\varphi_{\mathbf{k}}}{2}} c_{-}^{\dagger}(\mathbf{k})] |0\rangle$, where $\theta_{\mathbf{k}} = \pi - \theta_{-\mathbf{k}}$ and $\varphi_{\mathbf{k}} = \varphi_{-\mathbf{k}}$ to preserve the time-reversal symmetry. The SVP state breaks time-reversal symmetry, while the spin-valley-locked IVC state breaks the $U(1)$ valley-charge conservation. Importantly, as a result of a single valley occupancy, a SVP ground state at half-filling $\nu = 1$ could lead to the valley-polarized quantum anomalous Hall insulating state.

To study the stabilized ground state at $\nu = 1$, we performed the Hartree-Fock mean-field calculations. In the calculations, we projected the interactions onto the top-most moiré bands [9, 55, 56]. The details of the calculations can be found in SM Sec. III and Sec. IV [47]. Here, we summarize the numerical results in Fig. 3(b) to Fig. 3(f). Fig. 3(b) displays the energy difference of the IVC and SVP state $E_{IVC} - E_{SVP}$ as a function of twist angle θ and dielectric constant ϵ . It is shown that in a wide parameter range, the SVP state exhibits lower energy than the IVC state, being compatible with previous results in moiré superlattices of graphene [55, 56, 58]. Indeed, $E_{IVC} - E_{SVP} > 0$ can be shown analytically in the long-wave limit $qL_M \ll 1$ as shown in SM Sec. III [47]. To obtain the observed insulating QAH state, a gapped SVP state is needed, which happens when the strength of Coulomb interaction overcomes the band dispersion as highlighted in Fig. 3(b).

We also performed the Hartree-Fock mean-field calculations with finite pseudo-magnetic fields ($\Phi = \frac{\sqrt{3}}{2} B_0 L_M^2 \neq 0$) which enables the moiré bands to carry

finite Chern numbers. We found that the SVP state is still more stable than the IVC state in this case. As shown in the upper panel of Fig. 3(c), the energy difference of $E_{IVC} - E_{SVP}$ is almost insensitive to the increase in the strength of pseudo-magnetic fields. This is because the corresponding magnetic energy ϵ_B is much smaller than the Coulomb interacting strength (~ 100 meV). In contrast with the stability of the SVP state, the topology of the moiré bands is determined by specific pseudo-magnetic fields. As shown in the lower panel of Fig. 3(c), the SVP states acquired finite Chern numbers at some range of pseudo-magnetic fields. Therefore, by considering the effects of pseudo-magnetic fields and Coulomb interactions, we demonstrated the degeneracy of the two moiré bands $\xi_{\pm}(\mathbf{k})$ can be lifted (see Fig. 3(d)) and a single moiré band carrying a finite Chern number appears at half-filling (see Fig. 3(e)). As a result, moiré TMD heterobilayers can exhibit valley-polarized quantum anomalous Hall states.

Discussion.— It is important to note that another natural way to create nontrivial Chern bands is by reducing the energy offset of the valence bands of MoTe₂ and WSe₂ by applying a displacement field, such that the moiré bands of the two TMD materials can hybridize to open a topologically non-trivial gap [14, 49]. However, it is not certain if the relatively small displacement field (~ 0.5 V/nm) used in the experiment [34] can hybridize the moiré bands from MoTe₂ and WSe₂, which are expected to have an energy offset of 300meV [29, 34]. In the case of QAH effect observed at 3/4 filling in twisted

bilayer graphene, the non-trivial Chern bands are generated by the coupling between the aligned graphene moiré superlattices and the boron nitride substrate [4, 7, 55, 59–61]. In this work, we propose a new mechanism that pseudo-magnetic fields induced by lattice relaxation can cause topological band inversion for moiré bands originated from a single layer (such as the MoTe₂ layer). Our results in principle can be applicable to other TMD materials with pseudo-magnetic fields [38, 48, 62]. Our model also provides a basis for the study of other strongly interacting phases such as fractional Chern insulating states [63–66] in heterobilayer TMDs.

In the SM Sec. V [47], we go beyond the pseudo-magnetic field approximation and introduce an effective tight-binding model to describe the MoTe₂/WSe₂ heterobilayer with lattice relaxation. We demonstrate how lattice relaxation can cause gap closing and reopening and change the topology of the top moiré bands. Both the gap closing positions as well as the topology of bands of the effective tight-binding model are consistent with the results from the pseudomagnetic field description.

Acknowledgments.— The authors thank the discussions with Liang Fu, Adrian Po, and Berthold Jäck. K.T.L. acknowledges the support of the Croucher Foundation and HKRGC through RFS2021-6S03, C6025-19G, AoE/P-701/20, 16310520, 16310219 and 16309718. K.F.M. acknowledges the support of the Air Force Office of Scientific Research under award number FA9550-20-1-0219.

-
- [1] Y. Cao, V. Fatemi, A. Demir, S. Fang, S. L. Tomarken, J. Y. Luo, J. D. Sanchez-Yamagishi, K. Watanabe, T. Taniguchi, E. Kaxiras, R. C. Ashoori, and P. Jarillo-Herrero, *Nature* **556**, 80 (2018).
 - [2] Y. Cao, V. Fatemi, S. Fang, K. Watanabe, T. Taniguchi, E. Kaxiras, and P. Jarillo-Herrero, *Nature* **556**, 43 (2018).
 - [3] M. Yankowitz, S. Chen, H. Polshyn, Y. Zhang, K. Watanabe, T. Taniguchi, D. Graf, A. F. Young, and C. R. Dean, *Science* **363**, 1059 (2019).
 - [4] A. L. Sharpe, E. J. Fox, A. W. Barnard, J. Finney, K. Watanabe, T. Taniguchi, M. A. Kastner, and D. Goldhaber-Gordon, *Science* **365**, 605 (2019).
 - [5] A. Kerelsky, L. J. McGilly, D. M. Kennes, L. Xian, M. Yankowitz, S. Chen, K. Watanabe, T. Taniguchi, J. Hone, C. Dean, A. Rubio, and A. N. Pasupathy, *Nature* **572**, 95 (2019).
 - [6] Y. Xie, B. Lian, B. Jäck, X. Liu, C.-L. Chiu, K. Watanabe, T. Taniguchi, B. A. Bernevig, and A. Yazdani, *Nature* **572**, 101 (2019).
 - [7] M. Serlin, C. L. Tschirhart, H. Polshyn, Y. Zhang, J. Zhu, K. Watanabe, T. Taniguchi, L. Balents, and A. F. Young, *Science* **367**, 900 (2020).
 - [8] R. Bistritzer and A. H. MacDonald, *Proceedings of the National Academy of Sciences* **108**, 12233 (2011).
 - [9] H. C. Po, L. Zou, A. Vishwanath, and T. Senthil, *Phys. Rev. X* **8**, 031089 (2018).
 - [10] M. Koshino, N. F. Q. Yuan, T. Koretsune, M. Ochi, K. Kuroki, and L. Fu, *Phys. Rev. X* **8**, 031087 (2018).
 - [11] L. Wang, E.-M. Shih, A. Ghiotto, L. Xian, D. A. Rhodes, C. Tan, M. Claassen, D. M. Kennes, Y. Bai, B. Kim, K. Watanabe, T. Taniguchi, X. Zhu, J. Hone, A. Rubio, A. N. Pasupathy, and C. R. Dean, *Nature Materials* **19**, 861 (2020).
 - [12] Z. Zhang, Y. Wang, K. Watanabe, T. Taniguchi, K. Ueno, E. Tutuc, and B. J. LeRoy, *Nature Physics* **16**, 1093 (2020).
 - [13] M. H. Naik and M. Jain, *Phys. Rev. Lett.* **121**, 266401 (2018).
 - [14] F. Wu, T. Lovorn, E. Tutuc, I. Martin, and A. H. MacDonald, *Phys. Rev. Lett.* **122**, 086402 (2019).
 - [15] Z. Bi and L. Fu, *Nature Communications* **12**, 642 (2021).
 - [16] C. Zhang, C.-P. Chuu, X. Ren, M.-Y. Li, L.-J. Li, C. Jin, M.-Y. Chou, and C.-K. Shih, *Science Advances* **3** (2017), 10.1126/sciadv.1601459.
 - [17] Q. Tong, H. Yu, Q. Zhu, Y. Wang, X. Xu, and W. Yao, *Nature Physics* **13**, 356 (2017).
 - [18] F. Wu, T. Lovorn, E. Tutuc, and A. H. MacDonald, *Phys. Rev. Lett.* **121**, 026402 (2018).
 - [19] C. Jin, E. C. Regan, A. Yan, M. Iqbal Bakti Utama, D. Wang, S. Zhao, Y. Qin, S. Yang, Z. Zheng, S. Shi, K. Watanabe, T. Taniguchi, S. Tongay, A. Zettl, and

- F. Wang, *Nature* **567**, 76 (2019).
- [20] K. Tran, G. Moody, F. Wu, X. Lu, J. Choi, K. Kim, A. Rai, D. A. Sanchez, J. Quan, A. Singh, J. Embley, A. Zepeda, M. Campbell, T. Autry, T. Taniguchi, K. Watanabe, N. Lu, S. K. Banerjee, K. L. Silverman, S. Kim, E. Tutuc, L. Yang, A. H. MacDonald, and X. Li, *Nature* **567**, 71 (2019).
- [21] K. L. Seyler, P. Rivera, H. Yu, N. P. Wilson, E. L. Ray, D. G. Mandrus, J. Yan, W. Yao, and X. Xu, *Nature* **567**, 66 (2019).
- [22] Y. Shimazaki, I. Schwartz, K. Watanabe, T. Taniguchi, M. Kroner, and A. Imamoğlu, *Nature* **580**, 472 (2020).
- [23] Y. Tang, L. Li, T. Li, Y. Xu, S. Liu, K. Barmak, K. Watanabe, T. Taniguchi, A. H. MacDonald, J. Shan, and K. F. Mak, *Nature* **579**, 353 (2020).
- [24] E. C. Regan, D. Wang, C. Jin, M. I. Bakti Utama, B. Gao, X. Wei, S. Zhao, W. Zhao, Z. Zhang, K. Yumigeta, M. Blei, J. D. Carlström, K. Watanabe, T. Taniguchi, S. Tongay, M. Crommie, A. Zettl, and F. Wang, *Nature* **579**, 359 (2020).
- [25] Y. Xu, S. Liu, D. A. Rhodes, K. Watanabe, T. Taniguchi, J. Hone, V. Elser, K. F. Mak, and J. Shan, *Nature* **587**, 214 (2020).
- [26] X. Huang, T. Wang, S. Miao, C. Wang, Z. Li, Z. Lian, T. Taniguchi, K. Watanabe, S. Okamoto, D. Xiao, S.-F. Shi, and Y.-T. Cui, *Nature Physics* **17**, 715 (2021).
- [27] Y. Zhang, N. F. Q. Yuan, and L. Fu, *Phys. Rev. B* **102**, 201115 (2020).
- [28] C. Jin, Z. Tao, T. Li, Y. Xu, Y. Tang, J. Zhu, S. Liu, K. Watanabe, T. Taniguchi, J. C. Hone, L. Fu, J. Shan, and K. F. Mak, *Nature Materials* (2021), 10.1038/s41563-021-00959-8.
- [29] T. Li, S. Jiang, L. Li, Y. Zhang, K. Kang, J. Zhu, K. Watanabe, T. Taniguchi, D. Chowdhury, L. Fu, J. Shan, and K. F. Mak, *Nature* **597**, 350 (2021).
- [30] N. Morales-Durán, A. H. MacDonald, and P. Potasz, *Phys. Rev. B* **103**, L241110 (2021).
- [31] D. Xiao, G.-B. Liu, W. Feng, X. Xu, and W. Yao, *Phys. Rev. Lett.* **108**, 196802 (2012).
- [32] X. Xi, Z. Wang, W. Zhao, J.-H. Park, K. T. Law, H. Berger, L. Forró, J. Shan, and K. F. Mak, *Nature Physics* **12**, 139 (2016).
- [33] J. M. Lu, O. Zheliuk, I. Leermakers, N. F. Q. Yuan, U. Zeitler, K. T. Law, and J. T. Ye, *Science* **350**, 1353 (2015).
- [34] T. Li, S. Jiang, B. Shen, Y. Zhang, L. Li, T. Devakul, K. Watanabe, T. Taniguchi, L. Fu, J. Shan, and K. F. Mak, *arXiv e-prints*, arXiv:2107.01796 (2021), arXiv:2107.01796 [cond-mat.mes-hall].
- [35] C. L. Kane and E. J. Mele, *Phys. Rev. Lett.* **95**, 226801 (2005).
- [36] N. N. T. Nam and M. Koshino, *Phys. Rev. B* **96**, 075311 (2017).
- [37] H. Shi, Z. Zhan, Z. Qi, K. Huang, E. v. Veen, J. Á. Silva-Guillén, R. Zhang, P. Li, K. Xie, H. Ji, M. I. Katsnelson, S. Yuan, S. Qin, and Z. Zhang, *Nature Communications* **11**, 371 (2020).
- [38] V. V. Enaldiev, V. Zólyomi, C. Yelgel, S. J. Magorrian, and V. I. Fal'ko, *Phys. Rev. Lett.* **124**, 206101 (2020).
- [39] I. Maity, P. K. Maiti, H. R. Krishnamurthy, and M. Jain, *Phys. Rev. B* **103**, L121102 (2021).
- [40] S. J. Magorrian, V. V. Enaldiev, V. Zólyomi, F. Ferreira, V. I. Fal'ko, and D. A. Ruiz-Tijerina, *Phys. Rev. B* **104**, 125440 (2021).
- [41] A. Weston, Y. Zou, V. Enaldiev, A. Summerfield, N. Clark, V. Zólyomi, A. Graham, C. Yelgel, S. Magorrian, M. Zhou, J. Zultak, D. Hopkinson, A. Barinov, T. H. Bointon, A. Kretinin, N. R. Wilson, P. H. Beton, V. I. Fal'ko, S. J. Haigh, and R. Gorbachev, *Nature Nanotechnology* **15**, 592 (2020).
- [42] E. Li, J.-X. Hu, X. Feng, Z. Zhou, L. An, K. T. Law, N. Wang, and N. Lin, *Nature Communications* **12**, 5601 (2021).
- [43] H. Li, S. Li, M. H. Naik, J. Xie, X. Li, J. Wang, E. Regan, D. Wang, W. Zhao, S. Zhao, S. Kahn, K. Yumigeta, M. Blei, T. Taniguchi, K. Watanabe, S. Tongay, A. Zettl, S. G. Louie, F. Wang, and M. F. Crommie, *Nature Materials* **20**, 945 (2021).
- [44] N. Mounet, M. Gibertini, P. Schwaller, D. Campi, A. Merkys, A. Marrazzo, T. Sohier, I. E. Castelli, A. Ceperlotti, G. Pizzi, and N. Marzari, *Nature Nanotechnology* **13**, 246 (2018).
- [45] L. Meckbach, J. Hader, U. Huttner, J. Neuhaus, J. T. Steiner, T. Stroucken, J. V. Moloney, and S. W. Koch, *Phys. Rev. B* **101**, 075401 (2020).
- [46] M. Li, M. Z. Bellus, J. Dai, L. Ma, X. Li, H. Zhao, and X. C. Zeng, *Nanotechnology* **29**, 335203 (2018).
- [47] See supplementary Material for (1) Spinless time-reversal symmetry and the vanishing of Chern number; (2) Derivation of effective Hamiltonian through the perturbation theory; (3) Coulomb interaction and Hartree-Fock calculations; (4) Details for numerical calculations; (5) Effective tight-binding model calculation with lattice relaxation for moiré heterobilayer TMDs.
- [48] J. Mao, S. P. Milovanovic, M. Andelkovic, X. Lai, Y. Cao, K. Watanabe, T. Taniguchi, L. Covaci, F. M. Peeters, A. K. Geim, Y. Jiang, and E. Y. Andrei, *Nature* **584**, 215 (2020).
- [49] Y. Zhang, T. Devakul, and L. Fu, *Proceedings of the National Academy of Sciences* **118** (2021).
- [50] F. D. M. Haldane, *Phys. Rev. Lett.* **61**, 2015 (1988).
- [51] N. Levy, S. A. Burke, K. L. Meaker, M. Panlasigui, A. Zettl, F. Guinea, A. H. C. Neto, and M. F. Crommie, *Science* **329**, 544 (2010).
- [52] F. Guinea, M. I. Katsnelson, and A. K. Geim, *Nature Physics* **6**, 30 (2010).
- [53] J. Liu and X. Dai, *Phys. Rev. B* **103**, 035427 (2021).
- [54] P. Stepanov, I. Das, X. Lu, A. Fahimniya, K. Watanabe, T. Taniguchi, F. H. L. Koppens, J. Lischner, L. Levitov, and D. K. Efetov, *Nature* **583**, 375 (2020).
- [55] Y.-H. Zhang, D. Mao, Y. Cao, P. Jarillo-Herrero, and T. Senthil, *Phys. Rev. B* **99**, 075127 (2019).
- [56] J. Y. Lee, E. Khalaf, S. Liu, X. Liu, Z. Hao, P. Kim, and A. Vishwanath, *Nature Communications* **10**, 5333 (2019).
- [57] M. Xie and A. H. MacDonald, *Phys. Rev. Lett.* **124**, 097601 (2020).
- [58] C. Repellin, Z. Dong, Y.-H. Zhang, and T. Senthil, *Phys. Rev. Lett.* **124**, 187601 (2020).
- [59] G. Chen, A. L. Sharpe, E. J. Fox, Y.-H. Zhang, S. Wang, L. Jiang, B. Lyu, H. Li, K. Watanabe, T. Taniguchi, Z. Shi, T. Senthil, D. Goldhaber-Gordon, Y. Zhang, and F. Wang, *Nature* **579**, 56 (2020).
- [60] Y.-H. Zhang, D. Mao, and T. Senthil, *Phys. Rev. Research* **1**, 033126 (2019).
- [61] N. Bultinck, S. Chatterjee, and M. P. Zaletel, *Phys. Rev. Lett.* **124**, 166601 (2020).

- [62] D. Zhai and W. Yao, Phys. Rev. Materials **4**, 094002 (2020).
- [63] E. J. Bergholtz and Z. Liu, International Journal of Modern Physics B **27**, 1330017 (2013).
- [64] A. Abouelkomsan, Z. Liu, and E. J. Bergholtz, Phys. Rev. Lett. **124**, 106803 (2020).
- [65] P. J. Ledwith, G. Tarnopolsky, E. Khalaf, and A. Vishwanath, Phys. Rev. Research **2**, 023237 (2020).
- [66] C. Repellin and T. Senthil, Phys. Rev. Research **2**, 023238 (2020).
- [67] M. A. Cazalilla, H. Ochoa, and F. Guinea, Phys. Rev. Lett. **113**, 077201 (2014).
- [68] G.-B. Liu, W.-Y. Shan, Y. Yao, W. Yao, and D. Xiao, Phys. Rev. B **88**, 085433 (2013).
- [69] T. Fukui, Y. Hatsugai, and H. Suzuki, Journal of the Physical Society of Japan **74**, 1674 (2005).
- [70] M. Vozmediano, M. Katsnelson, and F. Guinea, Physics Reports **496**, 109 (2010).
- [71] S. Fang, S. Carr, M. A. Cazalilla, and E. Kaxiras, Phys. Rev. B **98**, 075106 (2018).
- [72] B. T. Zhou, C.-P. Zhang, and K. Law, Phys. Rev. Applied **13**, 024053 (2020).

Supplementary Material for “Valley-polarized Quantum Anomalous Hall State in Moiré MoTe₂/WSe₂ Heterobilayers”

Ying-Ming Xie,¹ Cheng-Ping Zhang¹, Jin-Xin Hu¹, Kin Fai Mak^{2,3,4}, K. T. Law^{1,*}

¹*Department of Physics, Hong Kong University of Science and Technology, Clear Water Bay, Hong Kong, China*

²*School of Applied and Engineering Physics, Cornell University, Ithaca, NY, USA*

³*Kavli Institute at Cornell for Nanoscale Science, Ithaca, NY, USA*

⁴*Laboratory of Atomic and Solid State Physics, Cornell University, Ithaca, NY, USA*

I. SPINLESS TIME-REVERSAL SYMMETRY AND THE VANISHING OF CHERN NUMBER

If there is no pseudo-magnetic field, as we discussed in the main text, there is an emergent spinless time-reversal symmetry $T' = \hat{K}$ with $T'\mathcal{H}_\tau(\mathbf{r})T'^{-1} = \mathcal{H}_\tau(\mathbf{r})$. In this section, we show such spinless time-reversal symmetry would enforce the Chern number of a moiré band to be zero.

We define the wavefunction as $\psi_{n,\tau,\mathbf{k}}(\mathbf{r}) = u_{n,\tau,\mathbf{k}}(\mathbf{r})e^{i\mathbf{k}\cdot\mathbf{r}}$, where n labels the band index, and τ is the valley index. The Berry curvature

$$\Omega(\mathbf{k}) = -i(\langle \partial_{k_x} u(\mathbf{k}) | \partial_{k_y} u(\mathbf{k}) \rangle - \langle \partial_{k_y} u(\mathbf{k}) | \partial_{k_x} u(\mathbf{k}) \rangle) \quad (\text{S1})$$

and the Chern number $C = \int_{\mathbf{k} \in B.Z.} \frac{d\mathbf{k}}{(2\pi)^2} \Omega(\mathbf{k})$. Under the spinless time-reversal symmetry $T' : u_{n,\tau}(\mathbf{k}) \mapsto u_{n,\tau}^*(-\mathbf{k})$ so that $T' : \Omega(\mathbf{k}) \mapsto -i(\langle \partial_{k_y} u(-\mathbf{k}) | \partial_{k_x} u(-\mathbf{k}) \rangle - \langle \partial_{k_x} u(-\mathbf{k}) | \partial_{k_y} u(-\mathbf{k}) \rangle) = -\Omega(-\mathbf{k})$. As the Hamiltonian is invariant under this spinless time-reversal symmetry, we thus obtain

$$\Omega(\mathbf{k}) = -\Omega(-\mathbf{k}). \quad (\text{S2})$$

Therefore, we have shown this emergent time-reversal symmetry T' enforces the Berry curvature to be odd in the Brillouin zone. As a result, the Chern number of a moiré band that is equal to the integral of the Berry curvature over the whole Brillouin zone vanishes.

II. DERIVATION OF EFFECTIVE HAMILTONIAN THROUGH THE PERTURBATION THEORY

A. Three-band effective model Hamiltonian near moiré Brillouin zone corners

The moiré Hamiltonian is

$$\mathcal{H}_\tau(\mathbf{r}) = -\frac{(\hat{\mathbf{p}} + \tau e\mathbf{A})^2}{2m^*} + V(\mathbf{r}), \quad (\text{S3})$$

where the moiré potential is

$$V(\mathbf{r}) = 2V_0 \sum_{j=1,3,5} \cos(\mathbf{G}_j \cdot \mathbf{r} + \phi) = \sum_j V(\mathbf{G}_j) e^{i\mathbf{G}_j \cdot \mathbf{r}}, \quad (\text{S4})$$

where $\mathbf{G}_j = \frac{4\pi}{\sqrt{3}L_M}(\cos(\frac{(j-1)\pi}{3}), \sin(\frac{(j-1)\pi}{3}))$. As discussed in the main text, we can take the corresponding gauge field of $B(\mathbf{r})$ as $\mathbf{A}(\mathbf{r}) = A_0[\mathbf{a}_2 \sin(\mathbf{G}_1 \cdot \mathbf{r}) - \mathbf{a}_1 \sin(\mathbf{G}_3 \cdot \mathbf{r}) - \mathbf{a}_3 \sin(\mathbf{G}_5 \cdot \mathbf{r})]$, where we chose the Coulomb gauge $\nabla \cdot \mathbf{A} = 0$, and define $\mathbf{a}_1 = (\frac{\sqrt{3}}{2}, \frac{1}{2})L_M$, $\mathbf{a}_2 = (0, 1)L_M$, $\mathbf{a}_3 = \mathbf{a}_2 - \mathbf{a}_1$, and $A_0 = \sqrt{3}B_0/4\pi$. This gauge field can be generated by a strain displacement field $\mathbf{u} = u_0[\mathbf{G}_1 \cos(\mathbf{G}_1 \cdot \mathbf{r}) + \mathbf{G}_3 \cos(\mathbf{G}_3 \cdot \mathbf{r}) + \mathbf{G}_5 \cos(\mathbf{G}_5 \cdot \mathbf{r})]$ with $u_0 = -\frac{3A_0L_M^3}{16\pi^2\alpha}$. It gives rise to a strain field $u_{ij}(\mathbf{r}) = (\partial_i u_j(\mathbf{r}) + \partial_j u_i(\mathbf{r}))/2$, which leads to the gauge field $\mathbf{A} = \alpha(2u_{xy}, u_{xx} - u_{yy})$ as desired. Note unlike the constant pseudo-magnetic fields considered in [67], here the pseudo-magnetic fields we consider are periodic, which take the same periodicity as the moiré potential, being motivated by a recent lattice relaxation calculation for moiré transition metal dichalcogenides [38].

It can be found in the presence of gauge potential

$$\mathcal{H}_\tau(\mathbf{r}) = -\frac{(\hat{\mathbf{p}} + \tau \frac{\Phi}{\Phi_0} \tilde{\mathbf{A}})^2}{2m} + V(\mathbf{r}) \approx -\frac{\hat{\mathbf{p}}^2}{2m} + \tau \gamma \tilde{\mathbf{A}} \cdot \mathbf{p} + V(\mathbf{r}), \quad (\text{S5})$$

where the quantum flux $\Phi_0 = \frac{h}{e}$, the flux $\Phi = \frac{\sqrt{3}}{2} B_0 L_M^2$, $\tilde{\mathbf{A}} = 4\pi \mathbf{A}(\mathbf{r}) / B_0 \sqrt{3} L_M$ and $\gamma = -\frac{\hbar \Phi}{m L_M \Phi_0}$, and we dropped \mathbf{A}^2 term here but it will be added in numerical calculations. In the following, we consider the moiré Hamiltonian at $+K$ valley: $\mathcal{H}_+(\mathbf{r})$, and the results for $-K$ valley is directly obtained with the time-reversal operation.

First, let us consider the case $\mathbf{A} = 0$. Because the three corners of moiré Brillouin are connected by the superlattice reciprocal vectors, using the plane waves $|\mathbf{k}\rangle = e^{i\mathbf{k}\cdot\mathbf{r}}$, the effective Hamiltonian near $\pm\kappa$ is written as

$$H_{\pm\kappa}(\mathbf{k}) = \begin{pmatrix} \epsilon_{\pm\kappa} \pm vk_y & V_0 e^{\pm i\phi} & V_0 e^{\mp i\phi} \\ V_0 e^{\mp i\phi} & \epsilon_{\pm\kappa} \pm v(-\frac{\sqrt{3}}{2}k_x - \frac{1}{2}k_y) & V_0 e^{\pm i\phi} \\ V_0 e^{\pm i\phi} & V_0 e^{\mp i\phi} & \epsilon_{\pm\kappa} \pm v(\frac{\sqrt{3}}{2}k_x - \frac{1}{2}k_y) \end{pmatrix}, \quad (\text{S6})$$

where $\epsilon_{\pm\kappa} = \epsilon_0 = -\kappa^2/2m^*$, $v = \kappa/m^*$. At the Brillouin zone corners, the eigenenergies and eigenwavefunctions are

$$\epsilon_1 = \epsilon_0 + 2V_0 \cos \phi, |\epsilon_1\rangle = \frac{1}{\sqrt{3}}(|\pm\kappa_1\rangle + |\pm\kappa_2\rangle + |\pm\kappa_3\rangle) \quad (\text{S7})$$

$$\epsilon_2 = \epsilon_0 + 2V_0 \cos(\frac{2\pi}{3} + \phi), |\epsilon_2\rangle = \frac{e^{i\frac{\pi}{2}}}{\sqrt{3}}(|\pm\kappa_1\rangle + e^{\pm i\frac{2\pi}{3}}|\pm\kappa_2\rangle + e^{\mp i\frac{2\pi}{3}}|\pm\kappa_3\rangle) \quad (\text{S8})$$

$$\epsilon_3 = \epsilon_0 + 2V_0 \cos(\frac{4\pi}{3} + \phi), |\epsilon_3\rangle = \frac{e^{-i\frac{\pi}{2}}}{\sqrt{3}}(|\pm\kappa_1\rangle + e^{\mp i\frac{2\pi}{3}}|\pm\kappa_2\rangle + e^{\pm i\frac{2\pi}{3}}|\pm\kappa_3\rangle) \quad (\text{S9})$$

When the gauge field is added, the gauge term $H'_{\pm\kappa}(\mathbf{A}) = \gamma \tilde{\mathbf{A}} \cdot \mathbf{p}$ becomes

$$H'_{\pm\kappa}(\tilde{\mathbf{A}}) \approx \begin{pmatrix} 0 & \pm\gamma \tilde{\mathbf{A}}(\pm\mathbf{G}_5) \cdot \boldsymbol{\kappa}_2 & \pm\gamma \tilde{\mathbf{A}}(\pm\mathbf{G}_6) \cdot \boldsymbol{\kappa}_3 \\ \pm\gamma \tilde{\mathbf{A}}(\pm\mathbf{G}_2) \cdot \boldsymbol{\kappa}_2 & 0 & \pm\gamma \tilde{\mathbf{A}}(\pm\mathbf{G}_1) \cdot \boldsymbol{\kappa}_3 \\ \pm\gamma \tilde{\mathbf{A}}(\pm\mathbf{G}_3) \cdot \boldsymbol{\kappa}_3 & \pm\gamma \tilde{\mathbf{A}}(\pm\mathbf{G}_4) \cdot \boldsymbol{\kappa}_3 & 0 \end{pmatrix}, \quad (\text{S10})$$

where

$$\boldsymbol{\kappa}_1 = \kappa(0, -1), \boldsymbol{\kappa}_2 = \kappa(\frac{\sqrt{3}}{2}, \frac{1}{2}), \boldsymbol{\kappa}_3 = \kappa(-\frac{\sqrt{3}}{2}, \frac{1}{2}), \quad (\text{S11})$$

and

$$\tilde{\mathbf{A}}(\mathbf{G}) = \frac{1}{S} \int d\mathbf{r} \tilde{\mathbf{A}}(\mathbf{r}) e^{-i\mathbf{G}\cdot\mathbf{r}} \quad (\text{S12})$$

with $\tilde{A}_x(\mathbf{r}) = -\frac{\sqrt{3}}{2} \sin(\mathbf{G}_3 \cdot \mathbf{r}) + \frac{\sqrt{3}}{2} \sin(\mathbf{G}_5 \cdot \mathbf{r})$, $\tilde{A}_y(\mathbf{r}) = \sin(\mathbf{G}_1 \cdot \mathbf{r}) - \frac{1}{2} \sin(\mathbf{G}_3 \cdot \mathbf{r}) - \frac{1}{2} \sin(\mathbf{G}_5 \cdot \mathbf{r})$, S denoting the sample area. As $\tilde{\mathbf{A}}(\mathbf{G}) = \mathbf{A}^*(-\mathbf{G})$, $H'_{\pm\kappa}(\mathbf{A})$ would have the same form. We can further obtain

$$H'_{\pm\kappa}(\mathbf{A}) = \begin{pmatrix} 0 & \frac{\kappa\gamma}{4i} & -\frac{\kappa\gamma}{4i} \\ -\frac{\kappa\gamma}{4i} & 0 & \frac{\kappa\gamma}{4i} \\ \frac{\kappa\gamma}{4i} & -\frac{\kappa\gamma}{4i} & 0 \end{pmatrix} \quad (\text{S13})$$

After projecting $H'_{\pm\kappa}(\mathbf{A})$ into the basis formed by $(|\epsilon_1\rangle, |\epsilon_2\rangle, |\epsilon_3\rangle)$, we find

$$H'_{\pm\kappa}(\mathbf{A}) = \frac{\sqrt{3}\kappa\gamma}{4} \begin{pmatrix} 0 & 0 & 0 \\ 0 & \pm 1 & 0 \\ 0 & 0 & \mp 1 \end{pmatrix} \quad (\text{S14})$$

Hence, in the basis spanned by $(|\epsilon_1\rangle, |\epsilon_2\rangle, |\epsilon_3\rangle)$, we can write it as

$$H_{\pm\kappa}^{eff}(\mathbf{k}) = \begin{pmatrix} \epsilon_0 + 2V_0 \cos \phi & \pm\frac{1}{2}v(k_x + ik_y) & \pm\frac{1}{2}v(k_x - ik_y) \\ \pm\frac{1}{2}v(k_x - ik_y) & \epsilon_0 + 2V_0 \cos(\frac{2\pi}{3} + \phi) \mp \epsilon_B & \pm\frac{1}{2}v(k_x + ik_y) \\ \pm\frac{1}{2}v(k_x + ik_y) & \mp\frac{1}{2}v(k_x - ik_y) & \epsilon_0 + 2V_0 \cos(\frac{4\pi}{3} + \phi) \pm \epsilon_B \end{pmatrix}, \quad (\text{S15})$$

where the magnetic energy that gives rise to the Dirac mass gap is given by

$$\epsilon_B = \frac{\sqrt{3}v}{4L_M} \frac{\Phi}{\Phi_0} = \frac{\hbar e B_0}{4m^*} \quad (\text{S16})$$

In the main text, we determined the topological phase transition boundaries with above three-band model and compared with the topological phase diagram from numerical calculations. The details for numerical calculations, including the diagonalization of full moiré Hamiltonian and Chern number, are summarized in Sec. IV of Supplementary Material (SM).

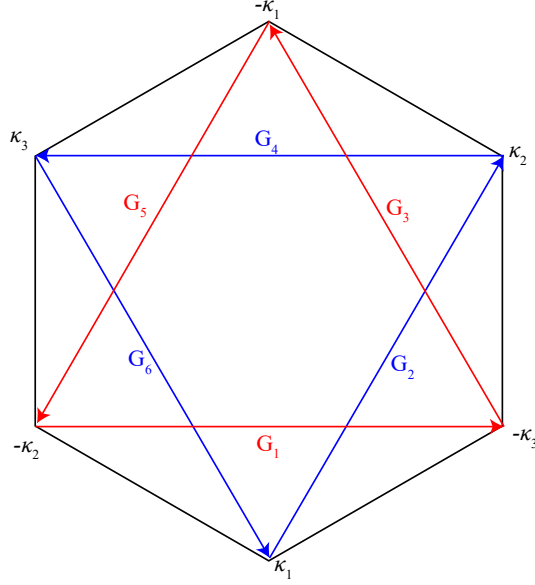


FIG. S1: A sketch of the moiré Brillouin zone and how the moiré Brillouin corners κ are connected by reciprocal lattice vectors G_j .

B. Four-band effective model Hamiltonian near moiré Brillouin zone boundary

In the main text of Fig. 2, it can be seen the phase transition boundaries that separates $C = \pm 1$ phase and $C = \mp 2$ phase, where Chern number changes ± 3 , are not captured by above three-band model. As shown in Fig. S2, where we calculated the moiré bands along moiré Brillouin zone boundary numerically (see black solid lines), we found it is gap closings at general points of moiré Brillouin zone boundary that drives this topological phase transition. Due to C_3 symmetry, there are three gap closing points at three $m\kappa$ lines related by C_3 symmetry, which enables the change of Chern number to be ± 3 .

To capture all the topological transitions, we derived an effective continuum model at the whole moiré boundary, denoting as B_j , instead of near only $\pm\kappa$. In the space $(|k_{B2}\rangle, |k_{B2} + G_3\rangle, |k_{B2} + G_4\rangle, |k_{B2} + G_5\rangle)$, after a similar derivation shown in previous part, we can obtain a four by four effective Hamiltonian for the whole moiré boundary:

$$H_{L_2}^{eff} = \begin{pmatrix} \epsilon(k_{B2}) & V_0 e^{i\phi} & V_0 e^{-i\phi} & V_0 e^{-i\phi} \\ V_0 e^{-i\phi} & \epsilon(k_{B2}) & V_0 e^{i\phi} & V_0 e^{i\phi} \\ V_0 e^{i\phi} & V_0 e^{-i\phi} & \epsilon(k_{B2} + G_3) & 0 \\ V_0 e^{i\phi} & V_0 e^{-i\phi} & 0 & \epsilon(k_{B2} + G_5) \end{pmatrix} + \begin{pmatrix} 0 & \frac{\gamma}{2i} k_y & \frac{\gamma}{4i} (k_y + \frac{3}{2}\kappa) & \frac{\gamma}{4i} (k_y - \frac{3}{2}\kappa) \\ -\frac{\gamma}{2i} k_y & 0 & -\frac{\gamma}{4i} (k_y + \frac{3}{2}\kappa) & -\frac{\gamma}{4i} (k_y - \frac{3}{2}\kappa) \\ -\frac{\gamma}{4i} (k_y + \frac{3}{2}\kappa) & \frac{\gamma}{4i} (k_y + \frac{3}{2}\kappa) & 0 & 0 \\ -\frac{\gamma}{4i} (k_y - \frac{3}{2}\kappa) & \frac{\gamma}{4i} (k_y - \frac{3}{2}\kappa) & 0 & 0 \end{pmatrix}. \quad (S17)$$

The band dispersions given by this four-band continuum model are plotted in Fig. S2 as red dashed lines. It can be seen that it roughly captures the topology of numerically calculated moiré bands, although the bands gradually deviates from directly numerically calculated moiré bands at large pseudo-magnetic fields such as the case $\Phi/\Phi_0 = 0.8$ shown in Fig. S2.

C. The comparison between the bands from the continuum model and DFT bands

After we post this work, the DFT bands of AB-stacked $\text{MoTe}_2/\text{WSe}_2$ heterobilayer were presented in ref. [34, 49] recently. In this part, we present a comparison on the bands from our continuum model and from Zhang and Fu's DFT calculations (see Extended Data Figure 8 of ref. [34]). First, the valance band top of moiré bands in our work and Zhang and Fu's DFT bands are both originated from K/K' states of monolayer MoTe_2 . In other words, although we labelled the valance band maximum as γ , it does not mean the valance bands are originated from Γ states of monolayer MoTe_2 . It is important to note that the convention of labelling the high symmetry points of moiré Brillouin zone in our work and Zhang and Fu's DFT bands is different.

Specifically, we followed the Wu and MacDonald's continuum model's notation convention [18], where the valance bands top of K/K' states after folding into moiré Brillouin zone is labelled as lowercase γ , as shown in Fig. S3(a). In

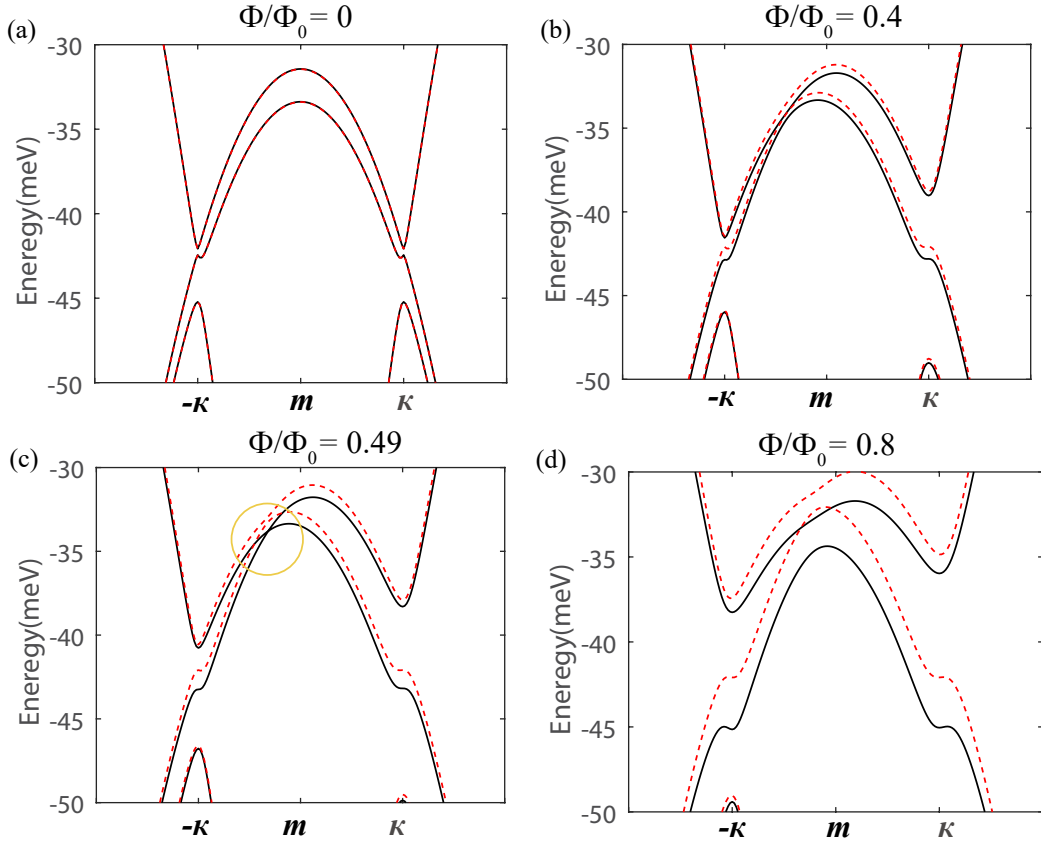


FIG. S2: (a) to (d) display the energy dispersion of top three moiré bands at moiré Brillouin zone boundary at $\Phi/\Phi_0 = 0, 0.4, 0.49, 0.8$ respectively. The red dashed lines are from the four-band effective model Hamiltonian Eq. (S17), while the black solid lines are from a direct diagonalization of the moiré Hamiltonian. Here, the moiré potential parameters $V_0 = 1$ meV, $\phi = 0.3\pi$ and angle $\theta = 0.53^\circ$ (note V_0 is the same as Fig. 2(a) but different from Fig. 1). It shows the gap closing point can happen at a general point of moiré Brillouin zone boundary beyond m and κ points. And this gives rise to the boundaries that separate $C = \pm 1$ phase and $C = \mp 2$ phase, where Chern number changes ± 3 , shown in the main text Fig. 2.

contrast, the valence bands top becomes $\pm K_m$ in the notation convention of Zhang and Fu's DFT bands as plotted in Fig. S3(c), inferring from their theoretical paper [49].

To compare the bands from our continuum model with their DFT bands more clearly, we replot the bands (Fig. S3(b)) following Zhang and Fu' convention. The resulting figure is Fig. S3(d), where the moiré bands from both original K/K' valleys are highlighted as red/blue colour. Regardless of a constant shift, it can be seen that the feature of top moiré bands at two valleys in Fig. S3(d) is quite consistent with the DFT bands (Extended Data Figure 8 of ref. [34]).

Another slight difference in the DFT bands of ref. [34] is that there are flats that originate from Γ -valley states of monolayer intersecting the more dispersive K/K' bands. Note that due to a large separation of K/K' and Γ valley in momentum space, the Γ -valley moiré bands and K/K' valley moiré bands are decoupled. K valley is much higher than Γ -valley for the monolayer WSe₂ and MoTe₂ (~ 300 meV difference for WSe₂ and 500 meV energy difference for MoTe₂ [68]), although the Γ -valley moiré bands are pushed up by the interlayer tunneling in this heterobilayer system. Nevertheless, the top moiré bands in DFT results are still contributed from K/K' valley, which give rise to the topological properties [34]. On the other hand, from the experimental side, there are no evidence that the Γ valley moiré bands would come near Fermi energy and affect the quantum anomalous Hall state. Therefore, in our continuum model, we directly focused on the moiré bands folded from K/K' states of monolayer MoTe₂. Γ -valley moiré bands are not relevant to our discussion concerning the topological properties from K/K' valley moiré bands.

It is worth noting that our continuum model captures both the AA and AB stacking, where MoTe₂ and WSe₂ are stacked in a parallel and antiparallel way respectively. The reason is that in both cases, it is the holes from MoTe₂

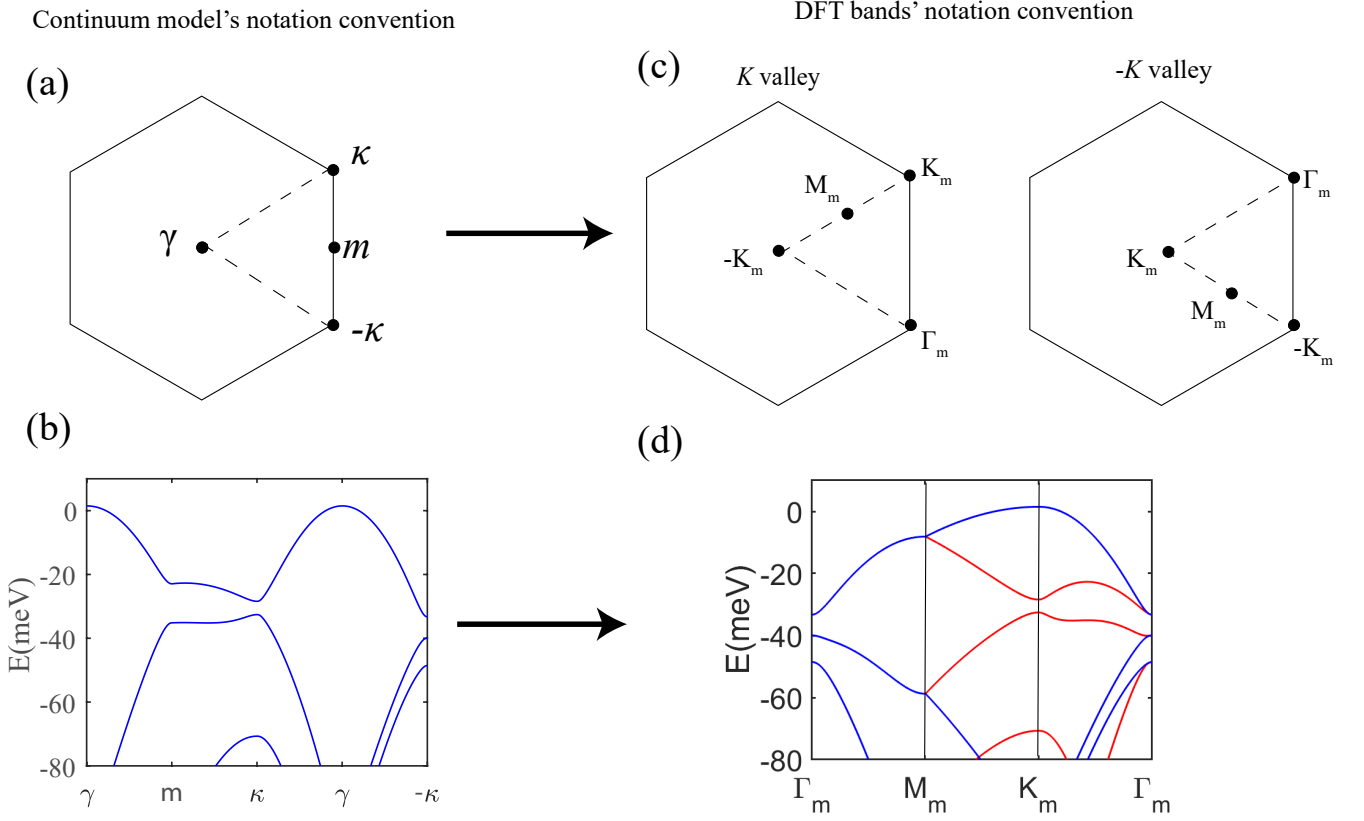


FIG. S3: (a) and (c) respectively show the notation convention of continuum model, DFT bands [34] labelling the high symmetry points of moiré Brillouin zone. (b) A copy of Fig. 1e in the main text. (d) is a plot of moiré bands of (b) using the DFT bands' notation convention. Here the moiré bands from K valley are in blue and K' valley are in red. In this convention, the top moiré bands from two valleys exhibit different energy at K_m which gives rise to a splitting. The features of top moiré bands are quite consistent with the ones in DFT bands (see Extended Data Figure 8 of ref. [34]).

layer are moving in the superlattice potential generated by the WSe₂ layer. However, the strength of moiré potential and pseudo-magnetic fields for two distinct stackings should be different. Importantly, in AB stacking due to the spin-valley locking at K/K'-valley, two layers would possess opposite spin in the same valley. As a result, the interlayer coupling is expected to be weaker in AB stacking, which results in a weaker moiré potential. As we showed in this work, to drive the system to be topological, the gap change caused by the pseudomagnetic fields should overcome the band gap opened by the periodic moiré potential. Therefore, we would expect pseudo-magnetic fields are easier to create topological moiré bands in AB stacking than AA stacking case. But from the symmetry point of view, it allows the topological moiré bands induced by pseudo-magnetic fields in AA-stacked MoTe₂/WSe₂ as well.

III. COULOMB INTERACTION AND HARTREE-FOCK CALCULATIONS

The Coulomb interaction is written as

$$H_{int} = \frac{1}{2} \int d\mathbf{r} \int d\mathbf{r}' c_{\sigma}^{\dagger}(\mathbf{r}) c_{\sigma'}^{\dagger}(\mathbf{r}') V(\mathbf{r} - \mathbf{r}') c_{\sigma'}(\mathbf{r}') c_{\sigma}(\mathbf{r}), \quad (\text{S18})$$

where σ is the spin index. Here, the screened Coulomb interaction $V(\mathbf{r}) = \frac{e^2}{4\pi\epsilon\epsilon_0} \frac{e^{-\lambda r}}{|\mathbf{r}|}$ and the electron creation operator

$$c_{\sigma}(\mathbf{r}) = \sum_{n, \mathbf{k} \in \text{B.Z.}} \psi_{n, \sigma, \mathbf{k}}(\mathbf{r}) c_{n, \sigma}(\mathbf{k}), \quad (\text{S19})$$

with $\psi_{n,\sigma,\mathbf{k}}(\mathbf{r}) = u_{n,\sigma,\mathbf{k}}(\mathbf{r})e^{i\mathbf{k}\cdot\mathbf{r}} = \frac{1}{\sqrt{S}} \sum_{\mathbf{G}} e^{i(\mathbf{G}+\mathbf{k})\cdot\mathbf{r}} u_{n,\sigma,\mathbf{k}}(\mathbf{G})$ as the Bloch wave function, n is the band index, \mathbf{k} is defined in the moiré Brillouin zone. Then Coulomb interaction in the momentum space reads

$$H_{int} = \frac{1}{2S} \sum_{\mathbf{k}_1, \mathbf{k}_2, \mathbf{k}_3, \mathbf{k}_4} V_{nn'mm'}(\mathbf{k}_1, \mathbf{k}_2, \mathbf{k}_3, \mathbf{k}_4) c_{n,\sigma}^\dagger(\mathbf{k}_1) c_{m,\sigma'}^\dagger(\mathbf{k}_2) c_{m',\sigma'}^\dagger(\mathbf{k}_3) c_{n',\sigma}(\mathbf{k}_4) \quad (\text{S20})$$

and

$$V_{nn'mm'}(\mathbf{k}_1, \mathbf{k}_2, \mathbf{k}_3, \mathbf{k}_4) = \frac{1}{S} \int d\mathbf{r} \int d\mathbf{r}' \psi_{n,\sigma,\mathbf{k}_1}^*(\mathbf{r}) \psi_{n',\sigma,\mathbf{k}_4}(\mathbf{r}) V(\mathbf{r} - \mathbf{r}') \psi_{m,\sigma',\mathbf{k}_2}^*(\mathbf{r}') \psi_{m',\sigma',\mathbf{k}_3}(\mathbf{r}') \quad (\text{S21})$$

$$= \sum_{\mathbf{q}, \mathbf{G}'_1, \mathbf{G}'_2, \mathbf{G}'_3, \mathbf{G}'_4} V(\mathbf{q}) \Lambda_{nn'}^\sigma(\mathbf{k}_1, \mathbf{k}_4) \Lambda_{mm'}^\sigma(\mathbf{k}_2, \mathbf{k}_3) \delta_{\mathbf{k}_1 + \mathbf{G}'_1, \mathbf{k}_4 + \mathbf{q} + \mathbf{G}'_4} \delta_{\mathbf{k}_2 + \mathbf{G}'_2, \mathbf{k}_3 + \mathbf{G}'_3 - \mathbf{q}}, \quad (\text{S22})$$

where $V(\mathbf{r}) = \frac{1}{S} \sum_{\mathbf{q}} V(\mathbf{q}) e^{i\mathbf{q}\cdot\mathbf{r}}$ with $V(\mathbf{q}) = \frac{e^2}{2\epsilon\epsilon_0 \sqrt{q^2 + \lambda^2}}$, $\Lambda_{nn'}^\sigma(\mathbf{k}_i, \mathbf{k}_j) = u_{\mathbf{k}_i}^\dagger(\mathbf{G}'_i) u_{\mathbf{k}_j}(\mathbf{G}'_j)$. Due to giant Ising spin-orbit coupling (SOC ~ 100 meV) near the valence band top of 2H-type transition metal dichalcogenide, the spin and valley are locked together, and thus we can replace the spin index σ with valley index τ . Then we obtain the Coulomb interaction as

$$H_{int} = \frac{1}{2S} \sum_{\mathbf{k}, \mathbf{k}', \mathbf{q}} V(\mathbf{q}) \Lambda_{nn'}^\tau(\mathbf{k} + \mathbf{q}, \mathbf{k}) \Lambda_{mm'}^{\tau'}(\mathbf{k}' - \mathbf{q}, \mathbf{k}') c_{n,\tau}^\dagger(\mathbf{k} + \mathbf{q}) c_{m,\tau'}^\dagger(\mathbf{k}' - \mathbf{q}) c_{m',\tau'}(\mathbf{k}') c_{n',\tau}(\mathbf{k}). \quad (\text{S23})$$

Note \mathbf{q} is defined in R^2 so that $\mathbf{k} \pm \mathbf{q}$ can exceeds the first Brillouin and in the calculation, it needs to be projected back to the first Brillouin zone as $\mathbf{k} \pm \mathbf{q} = \mathbf{G}'(\mathbf{k} \pm \mathbf{q}) + \mathbf{p}(\mathbf{k} \pm \mathbf{q})$, being equivalent to adjust \mathbf{G}'_j in Eq. (S22). Especially, after this projection, the form factor is given by

$$\Lambda_{nn'}^\tau(\mathbf{k} \pm \mathbf{q}, \mathbf{k}) = \sum_{\mathbf{G}} u_{\mathbf{p}(\mathbf{k} \pm \mathbf{q}), \tau}^\dagger(\mathbf{G} + \mathbf{G}'(\mathbf{k} \pm \mathbf{q})) u_{\mathbf{k}, \tau}(\mathbf{G}) \equiv \langle u_{n,\tau, \mathbf{k} \pm \mathbf{q}} | u_{n,\tau, \mathbf{k}} \rangle. \quad (\text{S24})$$

It can be seen that the intervalley Hund's coupling [56] is suppressed by the Ising SOC. From the definition, $\Lambda_{nn'}^\tau(\mathbf{k}_1, \mathbf{k}_2) = (\Lambda_{n'n}^\tau(\mathbf{k}_2, \mathbf{k}_1))^*$ and the time-reversal symmetry requires $\Lambda_{nn'}^\tau(\mathbf{k}_1, \mathbf{k}_2) = \Lambda_{n'n}^{-\tau}(-\mathbf{k}_2, -\mathbf{k}_1)$.

A. Hartree-Fock mean-field approximation with a simple form of Coulomb interaction

Next, let us perform the Hartree-Fock mean-field approximation. We first assume a simple form of interaction as

$$H_{int} = \frac{g}{2N} \sum_{\mathbf{k}, \mathbf{k}', \mathbf{q}} c_\tau^\dagger(\mathbf{k} + \mathbf{q}) c_{\tau'}^\dagger(\mathbf{k}' - \mathbf{q}) c_{\tau'}(\mathbf{k}') c_\tau(\mathbf{k}), \quad (\text{S25})$$

where the interaction effects on the top moiré bands is studied and the the interaction strength is taken as g , N is the number of moiré unit cells. A more complete form will be discussed later. Then we define the expectation value

$$\Delta_{\tau\tau'}(\mathbf{k}, \mathbf{k}') = \langle c_\tau^\dagger(\mathbf{k}) c_{\tau'}(\mathbf{k}') \rangle, \quad (\text{S26})$$

which is assumed to be diagonal in momentum space, i.e., $\Delta_{\tau\tau'}(\mathbf{k}, \mathbf{k}') = \Delta_{\tau\tau'}(\mathbf{k}) \delta_{\mathbf{k}, \mathbf{k}'}$.

The constraint for the order parameters are

$$\text{filling} : \quad \frac{1}{N} \sum_{\mathbf{k}} \text{tr}[\Delta(\mathbf{k})] = \nu. \quad (\text{S27})$$

$$\text{Symmetry} : \quad C_3 : \Delta(\mathbf{k}) \mapsto \Delta(C_3 \mathbf{k}) \quad (\text{S28})$$

$$T : \Delta(\mathbf{k}) \mapsto \tau_x \Delta^*(-\mathbf{k}) \tau_x \quad (\text{S29})$$

where $C_3 = \tau_0$ is the three-fold rotational symmetry, $T = \tau_x K$ is the time-reversal symmetry.

We expand the H_{int} in a mean-field manner:

$$\begin{aligned} H_{int}^{MF} \approx & \frac{g}{2N} \sum_{\mathbf{k}, \mathbf{k}', \mathbf{q}} c_\tau^\dagger(\mathbf{k} + \mathbf{q}) c_\tau(\mathbf{k}) \langle c_{\tau'}^\dagger(\mathbf{k}' - \mathbf{q}) c_{\tau'}(\mathbf{k}') \rangle + \langle c_\tau^\dagger(\mathbf{k} + \mathbf{q}) c_\tau(\mathbf{k}) \rangle c_{\tau'}^\dagger(\mathbf{k}' - \mathbf{q}) c_{\tau'}(\mathbf{k}') - \\ & \langle c_\tau^\dagger(\mathbf{k} + \mathbf{q}) c_\tau(\mathbf{k}) \rangle \langle c_{\tau'}^\dagger(\mathbf{k}' - \mathbf{q}) c_{\tau'}(\mathbf{k}') \rangle - \langle c_\tau^\dagger(\mathbf{k} + \mathbf{q}) c_{\tau'}(\mathbf{k}') \rangle c_{\tau'}^\dagger(\mathbf{k}' - \mathbf{q}) c_\tau(\mathbf{k}) - c_\tau^\dagger(\mathbf{k} + \mathbf{q}) c_{\tau'}(\mathbf{k}') \langle c_{\tau'}^\dagger(\mathbf{k}' - \mathbf{q}) c_\tau(\mathbf{k}) \rangle + \\ & \langle c_\tau^\dagger(\mathbf{k} + \mathbf{q}) c_{\tau'}(\mathbf{k}') \rangle \langle c_{\tau'}^\dagger(\mathbf{k}' - \mathbf{q}) c_\tau(\mathbf{k}) \rangle. \end{aligned} \quad (\text{S30})$$

The first three terms are the Hartree contributions, which is assumed to be finite only at $\mathbf{q} = 0$, and the last three terms are the Fock contributions. In a homogeneous electron gas, the Hartree contributions are canceled by the direct interaction with the positive background, and such contributions are determined by the local density of electrons and should not be sensitive to the specific order. Thus, the Fock terms are usually kept for our purpose. Then we obtain

$$H_{int}^{MF} \approx -g \sum_{\mathbf{k}} c_{\tau'}^\dagger(\mathbf{k}) \Delta_{\tau'\tau}^T c_\tau(\mathbf{k}) + \frac{gN}{2} \text{tr}(\Delta^2). \quad (\text{S31})$$

(1) the spin-valley-polarized (SVP) state. The time-reversal symmetry is broken. The order parameter for the valley-polarized states are

$$\Delta(\mathbf{k}) = \Delta_0(\mathbf{k})\tau_0 + \Delta_z(\mathbf{k})\tau_z. \quad (\text{S32})$$

We can define the macroscopic mean-field order parameters as

$$\Delta_0 = \frac{1}{N} \sum_{\mathbf{k}} \Delta_0(\mathbf{k}), \Delta_z = \frac{1}{N} \sum_{\mathbf{k}} \Delta_z(\mathbf{k}). \quad (\text{S33})$$

As a result, $\Delta_0 = 1/2$ at half-filling. And we consider interaction is much larger than bandwidth so that only one band is filled in near half-filling. In this case, the self-consistent equation reads

$$\Delta_0 + \Delta_z = \frac{1}{N} \sum_{\mathbf{k}} \Delta_{++}(\mathbf{k}) = 1 \quad (\text{S34})$$

$$\Delta_0 - \Delta_z = \frac{1}{N} \sum_{\mathbf{k}} \Delta_{--}(\mathbf{k}) = 0. \quad (\text{S35})$$

This gives $\Delta_z = 1/2$. The energy for the spin valley-polarized states are assumed to be

$$E_{SVP} = \sum_{\mathbf{k}} \xi_+(\mathbf{k}) - gN/2. \quad (\text{S36})$$

(2) the spin-valley-locked intervalley coherent (IVC) state (we will simply refer it as IVC state in the later discussions). The valley $U_v(1)$ symmetry is broken.

The order parameter for the valley-polarized states are assumed to be

$$\Delta(\mathbf{k}) = \begin{pmatrix} \Delta_0(\mathbf{k}) & \Delta_1(\mathbf{k}) \\ \Delta_1^*(\mathbf{k}) & \Delta_0(\mathbf{k}) \end{pmatrix}. \quad (\text{S37})$$

Here, $\Delta_0(\mathbf{k})$ is real, while $\Delta_1(\mathbf{k})$ is complex. We define $\Delta_1 = |\Delta_1|e^{i\varphi} = \frac{1}{N} \sum_{\mathbf{k}} \Delta_1(\mathbf{k})$. The mean-field Hamiltonian becomes

$$H_{MF} = \sum_{\mathbf{k}} (\xi_\tau(\mathbf{k}) - g\Delta_0) c_\tau^\dagger(\mathbf{k}) c_\tau(\mathbf{k}) - g \sum_{\mathbf{k}} (\Delta_1^* c_+^\dagger(\mathbf{k}) c_-(\mathbf{k}) + \Delta_1 c_-^\dagger(\mathbf{k}) c_+(\mathbf{k})) + gN(\Delta_0^2 + |\Delta_1|^2). \quad (\text{S38})$$

This mean-field Hamiltonian is diagonalized with a unitary transformation:

$$\begin{aligned} c_+(\mathbf{k}) &= \cos \frac{\theta_{\mathbf{k}}}{2} e^{-i\frac{\varphi}{2}} \gamma_+(\mathbf{k}) + \sin \frac{\theta_{\mathbf{k}}}{2} e^{-i\frac{\varphi}{2}} \gamma_-(\mathbf{k}), \\ c_-(\mathbf{k}) &= -\sin \frac{\theta_{\mathbf{k}}}{2} e^{i\frac{\varphi}{2}} \gamma_+(\mathbf{k}) + \cos \frac{\theta_{\mathbf{k}}}{2} e^{i\frac{\varphi}{2}} \gamma_-(\mathbf{k}), \end{aligned} \quad (\text{S39})$$

where

$$\cos \theta_{\mathbf{k}} = \frac{\xi_a(\mathbf{k})}{\sqrt{\xi_a^2(\mathbf{k}) + g^2 N^2 |\Delta_1|^2}}, \sin \theta_{\mathbf{k}} = \frac{gN|\Delta_1|}{\sqrt{\xi_a^2(\mathbf{k}) + g^2 N^2 |\Delta_1|^2}}, \quad (\text{S40})$$

and we denote $\xi_{s(a)}(\mathbf{k}) = (\xi_+(\mathbf{k}) \pm \xi_-(\mathbf{k}))/2$. After this transformation, the mean field Hamiltonian becomes

$$H_{MF} = \sum_{\mathbf{k}} E_+(\mathbf{k}) \gamma_+^\dagger(\mathbf{k}) \gamma_+(\mathbf{k}) + E_-(\mathbf{k}) \gamma_-^\dagger(\mathbf{k}) \gamma_-(\mathbf{k}) + gN(\Delta_0^2 + |\Delta_1|^2). \quad (\text{S41})$$

Here, the eigenenergies $E_{\pm}(\mathbf{k})$ are given by

$$E_{\pm}(\mathbf{k}) = \xi_s(\mathbf{k}) - gN\Delta_0 \pm \sqrt{(\xi_a(\mathbf{k}))^2 + g^2N^2|\Delta_1|^2}. \quad (\text{S42})$$

The self-consistent equation is

$$\Delta_1 = \frac{1}{N} \sum_{\mathbf{k}} \langle c_+^\dagger(\mathbf{k}) c_-(\mathbf{k}) \rangle = \frac{\Delta_1}{2N} \sum_{\mathbf{k}} \sin \theta_{\mathbf{k}} \langle -\gamma_+^\dagger(\mathbf{k}) \gamma_+(\mathbf{k}) + \gamma_-^\dagger(\mathbf{k}) \gamma_-(\mathbf{k}) \rangle \quad (\text{S43})$$

At half-filling, only the $E_-(\mathbf{k})$ bands are filled. The self-consistent equation is simplified as

$$|\Delta_1| = \frac{1}{2} \sum_{\mathbf{k}} \frac{g|\Delta_1|}{\sqrt{\xi_a^2(\mathbf{k}) + g^2N^2|\Delta_1|^2}}. \quad (\text{S44})$$

When the interaction is much larger than bandwidth, we can obtain $|\Delta_1| \approx 1/2$. The filling constraint further gives $\Delta_0 = 1/2$. Hence, the energy for the IVC state is approximated as

$$E_{IVC} = \sum_{\mathbf{k}} \xi_s(\mathbf{k}) - \sqrt{\xi_a^2(\mathbf{k}) + g^2N^2/4}. \quad (\text{S45})$$

The energy difference between the SVP states and the IVC states is

$$\delta E = E_{SVP} - E_{IVC} = \sum_{\mathbf{k}} \sqrt{\xi_a^2(\mathbf{k}) + g^2N^2/4} - gN/2 > 0 \quad (\text{S46})$$

Therefore, without considering the form factor, which encodes the information of the nontrivial wave-function, the states are tend to form the IVC states instead of SVP state.

B. Hartree-Fock mean-field approximation with a more general form of Coulomb interaction

Next, let us consider a more general form of Coulomb interaction:

$$H_{int} = \frac{V_0}{2N} \sum_{\mathbf{k}, \mathbf{k}', \mathbf{q}} v_{\mathbf{q}} \Lambda^\tau(\mathbf{k} + \mathbf{q}, \mathbf{k}) \Lambda^{\tau'}(\mathbf{k}' - \mathbf{q}, \mathbf{k}') c_\tau^\dagger(\mathbf{k} + \mathbf{q}) c_{\tau'}^\dagger(\mathbf{k}' - \mathbf{q}) c_{\tau'}(\mathbf{k}') c_\tau(\mathbf{k}), \quad (\text{S47})$$

where $V_0 = \frac{e^2}{2\epsilon\epsilon_0|\kappa|\Omega}$, the dimensionless screened Coulomb interaction is $v_{\mathbf{q}} = |\kappa|/\sqrt{\mathbf{q}^2 + \lambda^2}$, and only the top moiré band is considered. In a mean-field manner, the interaction is expanded as

$$\begin{aligned} H_{int}^{MF} \approx & \frac{V_0}{2N} \sum_{\mathbf{k}, \mathbf{k}', \mathbf{q}} v_{\mathbf{q}} \Lambda^\tau(\mathbf{k} + \mathbf{q}, \mathbf{k}) \Lambda^{\tau'}(\mathbf{k}' - \mathbf{q}, \mathbf{k}') [c_\tau^\dagger(\mathbf{k} + \mathbf{q}) c_\tau(\mathbf{k}) \langle c_{\tau'}^\dagger(\mathbf{k}' - \mathbf{q}) c_{\tau'}(\mathbf{k}') \rangle + \langle c_\tau^\dagger(\mathbf{k} + \mathbf{q}) c_\tau(\mathbf{k}) \rangle c_{\tau'}^\dagger(\mathbf{k}' - \mathbf{q}) c_{\tau'}(\mathbf{k}') - \\ & \langle c_\tau^\dagger(\mathbf{k} + \mathbf{q}) c_\tau(\mathbf{k}) \rangle \langle c_{\tau'}^\dagger(\mathbf{k}' - \mathbf{q}) c_{\tau'}(\mathbf{k}') \rangle - \langle c_\tau^\dagger(\mathbf{k} + \mathbf{q}) c_{\tau'}(\mathbf{k}') \rangle c_{\tau'}^\dagger(\mathbf{k}' - \mathbf{q}) c_\tau(\mathbf{k}) - c_\tau^\dagger(\mathbf{k} + \mathbf{q}) c_{\tau'}(\mathbf{k}') \langle c_{\tau'}^\dagger(\mathbf{k}' - \mathbf{q}) c_\tau(\mathbf{k}) \rangle + \\ & \langle c_\tau^\dagger(\mathbf{k} + \mathbf{q}) c_{\tau'}(\mathbf{k}') \rangle \langle c_{\tau'}^\dagger(\mathbf{k}' - \mathbf{q}) c_\tau(\mathbf{k}) \rangle]. \end{aligned} \quad (\text{S48})$$

To make the Coulomb interaction Hamiltonian more compact, let us define the Hartree and Fock order parameters:

$$\Delta_{\tau\tau'}^H(\mathbf{G}) = \frac{1}{N} \sum_{\mathbf{k}'} v_{\mathbf{G}} \Lambda^\tau(\mathbf{k}' + \mathbf{G}, \mathbf{k}') \langle c_\tau^\dagger(\mathbf{k}' + \mathbf{G}) c_{\tau'}(\mathbf{k}') \rangle \delta_{\tau\tau'}, \quad (\text{S49})$$

$$\Delta_{\tau\tau'}^F(\mathbf{k}, \mathbf{G}) = \frac{1}{N} \sum_{\mathbf{k}'} v_{\mathbf{k}' - \mathbf{k} + \mathbf{G}} \Lambda^\tau(\mathbf{k}' + \mathbf{G}, \mathbf{k}) \Lambda^{\tau'}(\mathbf{k} - \mathbf{G}, \mathbf{k}') \langle c_\tau^\dagger(\mathbf{k}' + \mathbf{G}) c_{\tau'}(\mathbf{k}') \rangle \quad (\text{S50})$$

With these definitions, we rewrite the first three Hartree terms as

$$H_{MF}^H \approx V_0 \sum_{\mathbf{k}} \sum_{\mathbf{G}} \text{tr}[\Delta^H(\mathbf{G})] \Lambda^\tau(\mathbf{k} - \mathbf{G}, \mathbf{k}) c_\tau^\dagger(\mathbf{k} - \mathbf{G}) c_\tau(\mathbf{k}) - \frac{NV_0}{2} \sum_{\mathbf{G}} \frac{\text{tr}[\Delta^H(\mathbf{G})] \text{tr}[\Delta^H(-\mathbf{G})]}{v_{\mathbf{G}}}. \quad (\text{S51})$$

Note the Hartree terms at $\mathbf{G} = 0$ are still considered to be canceled by some positive charge background. The next three are Fock terms:

$$H_{MF}^F \approx -V_0 \sum_{\mathbf{k}} \sum_{\mathbf{G}} c_{\tau}^{\dagger}(\mathbf{k} - \mathbf{G}) [\Delta^F(\mathbf{k}, \mathbf{G})]_{\tau\tau'}^T c_{\tau'}(\mathbf{k}) \quad (\text{S52})$$

$$+ \frac{V_0}{2N} \sum_{\mathbf{k}, \mathbf{k}', \mathbf{G}} v_{\mathbf{k}' - \mathbf{k} + \mathbf{G}} \Lambda^{\tau}(\mathbf{k}' + \mathbf{G}, \mathbf{k}) \Lambda^{\tau'}(\mathbf{k} - \mathbf{G}, \mathbf{k}') \langle c_{\tau}^{\dagger}(\mathbf{k}' + \mathbf{G}) c_{\tau'}(\mathbf{k}') \rangle \langle c_{\tau'}^{\dagger}(\mathbf{k} - \mathbf{G}) c_{\tau}(\mathbf{k}) \rangle. \quad (\text{S53})$$

Since we always do the calculation in the first Brillouin zone, $c^{\dagger}(\mathbf{k} \pm \mathbf{G})$ needs to be projected back to the first Brillouin zone as mentioned previously. After this projection, we arrive at a mean-field Hamiltonian as

$$H_{MF} \approx \sum_{\mathbf{k}} c_{\tau}^{\dagger}(\mathbf{k}) (\xi_{\tau}(\mathbf{k}) + V_0 \sum_{\mathbf{G}} \text{tr}[\Delta^H(\mathbf{G})] \Lambda^{\tau}(\mathbf{k} - \mathbf{G}, \mathbf{k})) c_{\tau}(\mathbf{k}) - V_0 \sum_{\mathbf{k}} \sum_{\mathbf{G}} c_{\tau}^{\dagger}(\mathbf{k}) [\Delta^F(\mathbf{k}, \mathbf{G})]_{\tau\tau'}^T c_{\tau'}(\mathbf{k}) \\ - \frac{NV_0}{2} \sum_{\mathbf{G}} \frac{\text{tr}[\Delta^H(\mathbf{G})] \text{tr}[\Delta^H(-\mathbf{G})]}{v_{\mathbf{G}}} + \frac{V_0}{2N} \sum_{\mathbf{k}, \mathbf{k}', \mathbf{G}} v_{\mathbf{k}' - \mathbf{k} + \mathbf{G}} \text{tr}[\Lambda(\mathbf{k}' + \mathbf{G}, \mathbf{k}) \Delta(\mathbf{k}') \Lambda(\mathbf{k} - \mathbf{G}, \mathbf{k}') \Delta(\mathbf{k})], \quad (\text{S54})$$

where

$$\Delta_{\tau\tau'}^H(\mathbf{G}) = \frac{1}{N} \sum_{\mathbf{k}'} v_{\mathbf{G}} \Lambda^{\tau}(\mathbf{k}' + \mathbf{G}, \mathbf{k}') \langle c_{\tau}^{\dagger}(\mathbf{k}' + \mathbf{G}) c_{\tau'}(\mathbf{k}') \rangle \delta_{\tau\tau'}, \quad (\text{S55})$$

$$\Delta_{\tau\tau'}^F(\mathbf{k}, \mathbf{G}) = \frac{1}{N} \sum_{\mathbf{k}'} v_{\mathbf{k}' - \mathbf{k} + \mathbf{G}} \Lambda^{\tau}(\mathbf{k}' + \mathbf{G}, \mathbf{k}) \Lambda^{\tau'}(\mathbf{k} - \mathbf{G}, \mathbf{k}') \langle c_{\tau}^{\dagger}(\mathbf{k}' + \mathbf{G}) c_{\tau'}(\mathbf{k}') \rangle \quad (\text{S56})$$

and the form factor is given by

$$\Lambda^{\tau}(\mathbf{k} \pm \mathbf{G}, \mathbf{k}) = \sum_{\mathbf{G}'} u_{\mathbf{k}, \tau}^{\dagger}(\mathbf{G}' \pm \mathbf{G}) u_{\mathbf{k}, \tau}(\mathbf{G}') \quad (\text{S57})$$

$$\Lambda^{\tau}(\mathbf{k}' \pm \mathbf{G}, \mathbf{k}) = \sum_{\mathbf{G}'} u_{\mathbf{k}', \tau}^{\dagger}(\mathbf{G}' \pm \mathbf{G}) u_{\mathbf{k}, \tau}(\mathbf{G}') \quad (\text{S58})$$

Let us consider the long-wave limit $qL_M \ll 1$ so that only $\mathbf{G} = 0$ in the sum needs to be considered. A more general case will be evaluated numerically as we will present later. In the long-wave limit case,

$$H_{MF} \approx \sum_{\mathbf{k}} c_{\tau}^{\dagger}(\mathbf{k}) \xi_{\tau}(\mathbf{k}) c_{\tau}(\mathbf{k}) - V_0 \sum_{\mathbf{k}} c_{\tau}^{\dagger}(\mathbf{k}) [\Delta^F(\mathbf{k})]_{\tau\tau'}^T c_{\tau'}(\mathbf{k}) + \frac{V_0}{2N} \sum_{\mathbf{k}, \mathbf{q}} v_{\mathbf{q}} \text{tr}[\Lambda(\mathbf{k} + \mathbf{q}, \mathbf{k}) \Delta(\mathbf{k} + \mathbf{q}) \Lambda(\mathbf{k}, \mathbf{k} + \mathbf{q}) \Delta(\mathbf{k})], \quad (\text{S59})$$

where

$$\Delta_{\tau\tau'}^F(\mathbf{k}) = \frac{1}{N} \sum_{\mathbf{q}} v_{\mathbf{q}} \Lambda^{\tau}(\mathbf{k} + \mathbf{q}, \mathbf{k}) \Delta_{\tau\tau'}(\mathbf{k} + \mathbf{q}) \Lambda^{\tau'}(\mathbf{k}, \mathbf{k} + \mathbf{q}). \quad (\text{S60})$$

For the SVP states, only one valley is occupied. Without loss of generality, we assume the $+$ valley is occupied, which gives the mean-field order parameter: $\Delta(\mathbf{k}) = 1/2(1 + \tau_z)$. The total energy of this SVP state is obtained as

$$E_{SVP} = \sum_{\mathbf{k}} [\xi_{+}(\mathbf{k}) - \frac{V_0}{2N} \sum_{\mathbf{q}} v_{\mathbf{q}} |\Lambda^{+}(\mathbf{k} + \mathbf{q}, \mathbf{k})|^2]. \quad (\text{S61})$$

Let us further consider the IVC states. In this case, the valley is not a good index. In this case, we take a general form of the order parameter:

$$\Delta(\mathbf{k}) = \begin{pmatrix} \langle c_{+}^{\dagger}(\mathbf{k}) c_{+}(\mathbf{k}) \rangle & \langle c_{+}^{\dagger}(\mathbf{k}) c_{-}(\mathbf{k}) \rangle \\ \langle c_{-}^{\dagger}(\mathbf{k}) c_{+}(\mathbf{k}) \rangle & \langle c_{-}^{\dagger}(\mathbf{k}) c_{-}(\mathbf{k}) \rangle \end{pmatrix} = \begin{pmatrix} \Delta_{++}(\mathbf{k}) & \Delta_{+-}(\mathbf{k}) \\ \Delta_{-+}(\mathbf{k}) & \Delta_{--}(\mathbf{k}) \end{pmatrix}. \quad (\text{S62})$$

The mean-field Hamiltonian Eq. (S59) becomes

$$H(\mathbf{k}) = \begin{pmatrix} \xi_{+}(\mathbf{k}) - \frac{V_0}{N} \sum_{\mathbf{q}} v_{\mathbf{q}} |\Lambda^{+}(\mathbf{k} + \mathbf{q}, \mathbf{k})|^2 \Delta_{++}(\mathbf{k} + \mathbf{q}) & -\frac{V_0}{N} \sum_{\mathbf{q}} v_{\mathbf{q}} \Lambda^{-}(\mathbf{k} + \mathbf{q}, \mathbf{k}) \Delta_{-+}(\mathbf{k} + \mathbf{q}) \Lambda^{+}(\mathbf{k}, \mathbf{k} + \mathbf{q}) \\ -\frac{V_0}{N} \sum_{\mathbf{q}} v_{\mathbf{q}} \Lambda^{+}(\mathbf{k} + \mathbf{q}, \mathbf{k}) \Delta_{+-}(\mathbf{k} + \mathbf{q}) \Lambda^{-}(\mathbf{k}, \mathbf{k} + \mathbf{q}) & \xi_{-}(\mathbf{k}) - \frac{V_0}{N} \sum_{\mathbf{q}} v_{\mathbf{q}} |\Lambda^{-}(\mathbf{k} + \mathbf{q}, \mathbf{k})|^2 \Delta_{--}(\mathbf{k} + \mathbf{q}) \end{pmatrix}. \quad (\text{S63})$$

Here, the basis is $(c_+(\mathbf{k}), c_-(\mathbf{k}))^T$. The last term in Eq. (S59) is a potential energy which will be added later. We can further parameterize $H(\mathbf{k})$ as

$$H(\mathbf{k}) = \begin{pmatrix} h_0(\mathbf{k}) + h_1(\mathbf{k}) & -h_2^*(\mathbf{k}) \\ -h_2(\mathbf{k}) & h_0(\mathbf{k}) - h_1(\mathbf{k}) \end{pmatrix}. \quad (\text{S64})$$

According to Eq. (S39), we can take the following transform to diagonalize $H(\mathbf{k})$:

$$\begin{aligned} c_+(\mathbf{k}) &= \cos \frac{\theta_{\mathbf{k}}}{2} e^{-i\frac{\varphi_{\mathbf{k}}}{2}} \gamma_+(\mathbf{k}) + \sin \frac{\theta_{\mathbf{k}}}{2} e^{-i\frac{\varphi_{\mathbf{k}}}{2}} \gamma_-(\mathbf{k}), \\ c_-(\mathbf{k}) &= -\sin \frac{\theta_{\mathbf{k}}}{2} e^{i\frac{\varphi_{\mathbf{k}}}{2}} \gamma_+(\mathbf{k}) + \cos \frac{\theta_{\mathbf{k}}}{2} e^{i\frac{\varphi_{\mathbf{k}}}{2}} \gamma_-(\mathbf{k}). \end{aligned} \quad (\text{S65})$$

After the unitary transform, we obtain the mean-field Hamiltonian

$$H = \sum_{\mathbf{k}} E_{\pm}(\mathbf{k}) \gamma_{\pm}^{\dagger}(\mathbf{k}) \gamma_{\pm}(\mathbf{k}). \quad (\text{S66})$$

The eigenenergies $E_{\pm}(\mathbf{k}) = h_0(\mathbf{k}) \pm \sqrt{h_1(\mathbf{k})^2 + |h_2(\mathbf{k})|^2}$. In the half-filling, only $E_-(\mathbf{k})$ is occupied. This also means $\langle \gamma_-^{\dagger}(\mathbf{k}) \gamma_-(\mathbf{k}) \rangle = 1$ and $\langle \gamma_+^{\dagger}(\mathbf{k}) \gamma_+(\mathbf{k}) \rangle = 0$. The parameters $\theta_{\mathbf{k}}$ and $\varphi_{\mathbf{k}}$ are determined by the following equations

$$\sin \theta_{\mathbf{k}} = \frac{|h_2(\mathbf{k})|}{\sqrt{h_1^2(\mathbf{k}) + |h_2(\mathbf{k})|^2}}, \cos \theta_{\mathbf{k}} = \frac{h_1(\mathbf{k})}{\sqrt{h_1^2(\mathbf{k}) + |h_2(\mathbf{k})|^2}}, \tan \varphi_{\mathbf{k}} = \frac{\text{Im}(h_2(\mathbf{k}))}{\text{Re}(h_2(\mathbf{k}))} \quad (\text{S67})$$

Here,

$$h_0(\mathbf{k}) = \frac{1}{2}(\xi_+(\mathbf{k}) + \xi_-(\mathbf{k})) - \frac{V_0}{2N} \sum_{\mathbf{q}} v_{\mathbf{q}} [|\Lambda^+(\mathbf{k} + \mathbf{q}, \mathbf{k})|^2 \sin^2 \frac{\theta_{\mathbf{k}+\mathbf{q}}}{2} + |\Lambda^-(\mathbf{k} + \mathbf{q}, \mathbf{k})|^2 \cos^2 \frac{\theta_{\mathbf{k}+\mathbf{q}}}{2}] \quad (\text{S68})$$

$$h_1(\mathbf{k}) = \frac{1}{2}(\xi_+(\mathbf{k}) - \xi_-(\mathbf{k})) - \frac{V_0}{2N} \sum_{\mathbf{q}} v_{\mathbf{q}} [|\Lambda^+(\mathbf{k} + \mathbf{q}, \mathbf{k})|^2 \sin^2 \frac{\theta_{\mathbf{k}+\mathbf{q}}}{2} - |\Lambda^-(\mathbf{k} + \mathbf{q}, \mathbf{k})|^2 \cos^2 \frac{\theta_{\mathbf{k}+\mathbf{q}}}{2}] \quad (\text{S69})$$

$$h_2(\mathbf{k}) = \frac{V_0}{2N} \sum_{\mathbf{q}} v_{\mathbf{q}} \sin \theta_{\mathbf{k}+\mathbf{q}} \Lambda^+(\mathbf{k} + \mathbf{q}, \mathbf{k}) \Lambda^-(\mathbf{k}, \mathbf{k} + \mathbf{q}) e^{i\varphi_{\mathbf{k}+\mathbf{q}}}. \quad (\text{S70})$$

Note we have replaced $\Delta(\mathbf{k})$ in the Hamiltonian as

$$\Delta(\mathbf{k}) = \begin{pmatrix} \sin^2 \frac{\theta_{\mathbf{k}}}{2} & \frac{1}{2} \sin \theta_{\mathbf{k}} e^{i\varphi_{\mathbf{k}}} \\ \frac{1}{2} \sin \theta_{\mathbf{k}} e^{-i\varphi_{\mathbf{k}}} & \cos^2 \frac{\theta_{\mathbf{k}}}{2} \end{pmatrix}, \quad (\text{S71})$$

which is obtained by substituting Eq. (S65) in Eq. (S62), and $\theta_{\mathbf{k}} = \pi - \theta_{-\mathbf{k}}$, $\varphi_{\mathbf{k}} = \varphi_{-\mathbf{k}}$ due to the the constraint of time reversal symmetry $T = \tau_x K$ given in Eq. S29. It can be seen that the half-filling constraint $\frac{1}{N} \sum_{\mathbf{k}} \text{tr}[\Delta(\mathbf{k})] = 1$ is satisfied. Moreover, there exhibits a gauge degree of freedom: $c_{\pm}(\mathbf{k}) \rightarrow c_{\pm}(\mathbf{k}) e^{\mp i\frac{\phi_{\mathbf{k}}}{2}}$. Under this gauge transform, $\Lambda^{\pm}(\mathbf{k} + \mathbf{q}, \mathbf{k}) \rightarrow \Lambda^{\pm}(\mathbf{k} + \mathbf{q}, \mathbf{k}) e^{\pm i(\phi_{\mathbf{k}} - \phi_{\mathbf{k}+\mathbf{q}})/2}$. This gauge phase will affect the $h_2(\mathbf{k})$, but will not affect the total energy.

If we approximate $\theta_{\mathbf{k}} \approx \theta_{\mathbf{k}+\mathbf{q}}$ considering $qL_M \ll 1$, the form of $E_{\pm}(\mathbf{k})$ can be simplified with the first equation in Eq. (S67), which is rewritten as

$$\sqrt{h_1^2(\mathbf{k}) + |h_2(\mathbf{k})|^2} = \frac{V_0}{2N} \sum_{\mathbf{q}} v_{\mathbf{q}} \Lambda^+(\mathbf{k} + \mathbf{q}, \mathbf{k}) \Lambda^-(\mathbf{k}, \mathbf{k} + \mathbf{q}) e^{i(\varphi_{\mathbf{k}+\mathbf{q}} - \varphi_{\mathbf{k}})}. \quad (\text{S72})$$

As only the band with energy $E_-(\mathbf{k})$ is filled in, we can obtain the total energy for the IVC states as

$$\begin{aligned} E_{IVC} &= \sum_{\mathbf{k}} h_0(\mathbf{k}) - \frac{V_0}{2N} \sum_{\mathbf{k}} \sum_{\mathbf{q}} v_{\mathbf{q}} \Lambda^+(\mathbf{k} + \mathbf{q}, \mathbf{k}) \Lambda^-(\mathbf{k}, \mathbf{k} + \mathbf{q}) e^{i(\varphi_{\mathbf{k}+\mathbf{q}} - \varphi_{\mathbf{k}})} + \frac{V_0}{2N} \sum_{\mathbf{k}} \sum_{\mathbf{q}} v_{\mathbf{q}} [\sin^2(\frac{\theta_{\mathbf{k}+\mathbf{q}}}{2}) \sin^2(\frac{\theta_{\mathbf{k}}}{2}) \\ &\quad + |\Lambda^+(\mathbf{k} + \mathbf{q}, \mathbf{k})|^2 + \cos^2(\frac{\theta_{\mathbf{k}+\mathbf{q}}}{2}) \cos^2(\frac{\theta_{\mathbf{k}}}{2}) |\Lambda^-(\mathbf{k} + \mathbf{q}, \mathbf{k})|^2 + \frac{1}{2} \sin(\theta_{\mathbf{k}}) \sin(\theta_{\mathbf{k}+\mathbf{q}}) \Lambda^+(\mathbf{k} + \mathbf{q}, \mathbf{k}) \Lambda^-(\mathbf{k}, \mathbf{k} + \mathbf{q}) e^{i(\varphi_{\mathbf{k}+\mathbf{q}} - \varphi_{\mathbf{k}})}]. \end{aligned} \quad (\text{S73})$$

The last potential term in Eq. (S59) is also added. Using the aforementioned approximation $\theta_{\mathbf{k}} \approx \theta_{\mathbf{k}+\mathbf{q}}$, we obtain

$$E_{IVC} = \sum_{\mathbf{k}} \xi_+(\mathbf{k}) - \frac{V_0}{2N} \sum_{\mathbf{k}, \mathbf{q}} \sin^2\left(\frac{\theta_{\mathbf{k}}}{2}\right) \cos^2\left(\frac{\theta_{\mathbf{k}}}{2}\right) [|\Lambda^+(\mathbf{k} + \mathbf{q}, \mathbf{k})|^2 + |\Lambda^-(\mathbf{k} + \mathbf{q}, \mathbf{k})|^2] \quad (\text{S74})$$

$$- \frac{V_0}{2N} \sum_{\mathbf{k}} \sum_{\mathbf{q}} v_{\mathbf{q}} \left(1 - \frac{1}{2} \sin^2(\theta_{\mathbf{k}})\right) \Lambda^+(\mathbf{k} + \mathbf{q}, \mathbf{k}) \Lambda^-(\mathbf{k}, \mathbf{k} + \mathbf{q}) e^{i(\varphi_{\mathbf{k}+\mathbf{q}} - \varphi_{\mathbf{k}})} \quad (\text{S75})$$

The lowest value of E_{IVC} is obtained as

$$E_{IVC}^{(0)} = \sum_{\mathbf{k}} \xi_+(\mathbf{k}) - \frac{V_0}{2N} \sum_{\mathbf{k}, \mathbf{q}} \sin^2\left(\frac{\theta_{\mathbf{k}}}{2}\right) \cos^2\left(\frac{\theta_{\mathbf{k}}}{2}\right) [|\Lambda^+(\mathbf{k} + \mathbf{q}, \mathbf{k})|^2 + |\Lambda^-(\mathbf{k} + \mathbf{q}, \mathbf{k})|^2] \quad (\text{S76})$$

$$- \frac{V_0}{2N} \sum_{\mathbf{k}} \sum_{\mathbf{q}} v_{\mathbf{q}} \left(1 - \frac{1}{2} \sin^2(\theta_{\mathbf{k}})\right) |\Lambda^+(\mathbf{k} + \mathbf{q}, \mathbf{k})| |\Lambda^-(\mathbf{k}, \mathbf{k} + \mathbf{q})|. \quad (\text{S77})$$

Therefore, the smallest energy difference between the SVP state and IVC state is

$$E_{IVC}^{(0)} - E_{SVP} \approx \frac{V_0}{4N} \sum_{\mathbf{k}, \mathbf{q}} \left(1 - \frac{1}{2} \sin^2 \theta_{\mathbf{k}}\right) (|\Lambda^+(\mathbf{k} + \mathbf{q}, \mathbf{k})| - |\Lambda^-(\mathbf{k}, \mathbf{k} + \mathbf{q})|)^2 > 0, \quad (\text{S78})$$

where $\sum_{\mathbf{k}} \sum_{\mathbf{q}} |\Lambda^+(\mathbf{k} + \mathbf{q}, \mathbf{k})|^2 = \sum_{\mathbf{k}} \sum_{\mathbf{q}} |\Lambda^-(\mathbf{k} + \mathbf{q}, \mathbf{k})|^2$ is used. It is found that the SVP states are favorable in this case, which is compatible with the result given in [55, 56]. Actually, we will present a more general formalism with finite \mathbf{G} later and we found the SVP state is still more stable than the IVC state.

IV. DETAILS FOR NUMERICAL CALCULATIONS

A. Diagonalization of the moiré Hamiltonian

The moiré Hamiltonian $\mathcal{H}_{\tau}(\mathbf{r}) = -\frac{(\hat{\mathbf{p}} + \tau e \mathbf{A})^2}{2m^*} + V(\mathbf{r})$ is diagonalized with the plane wave bases $\{|\mathbf{k} + \mathbf{G}\rangle\}$, where \mathbf{k} is defined within the moiré Brillouin zone, $\mathbf{G} = m\mathbf{G}_2 + n\mathbf{G}_3$ are the reciprocal lattice vectors for the moiré pattern, m, n are integer numbers. In this basis, the representation of the Hamiltonian is

$$\hat{H}_{\mathbf{k}}(\mathbf{G}', \mathbf{G}) = \langle \mathbf{k} + \mathbf{G}' | \mathcal{H}_{\tau}(\mathbf{r}) | \mathbf{k} + \mathbf{G} \rangle. \quad (\text{S79})$$

There are four different terms in the moiré Hamiltonian, i.e., $\mathcal{H}_{\tau}(\mathbf{r}) = -\hat{\mathbf{p}}^2/2m^* - \frac{\tau e}{m^*} \mathbf{A} \cdot \hat{\mathbf{p}} - e^2 \mathbf{A}^2/2m^* + V(\mathbf{r}) \equiv \mathcal{H}_{\hat{\mathbf{p}}^2} + \mathcal{H}_{\mathbf{A} \cdot \hat{\mathbf{p}}} + \mathcal{H}_{\mathbf{A}^2} + \mathcal{H}_V$. It is straightforward to obtain

$$\langle \mathbf{k} + \mathbf{G}' | \mathcal{H}_{\hat{\mathbf{p}}^2}(\mathbf{r}) | \mathbf{k} + \mathbf{G} \rangle = \frac{-(\mathbf{k} + \mathbf{G})^2}{2m^*} \delta_{\mathbf{G}, \mathbf{G}'}, \quad (\text{S80})$$

$$\langle \mathbf{k} + \mathbf{G}' | \mathcal{H}_V | \mathbf{k} + \mathbf{G} \rangle = V(\mathbf{G}' - \mathbf{G}), \quad (\text{S81})$$

$$\langle \mathbf{k} + \mathbf{G}' | \mathcal{H}_{\mathbf{A} \cdot \hat{\mathbf{p}}}(\mathbf{r}) | \mathbf{k} + \mathbf{G} \rangle = \tau \gamma \tilde{\mathbf{A}}(\mathbf{G}' - \mathbf{G}) \cdot (\mathbf{k} + \mathbf{G}), \quad (\text{S82})$$

$$\langle \mathbf{k} + \mathbf{G}' | \mathcal{H}_{\mathbf{A}^2} | \mathbf{k} + \mathbf{G} \rangle = -\frac{\hbar^2}{2m^* L_M^2} \frac{\Phi_0^2}{\Phi_0^2} \tilde{\mathbf{A}}^2(\mathbf{G}' - \mathbf{G}). \quad (\text{S83})$$

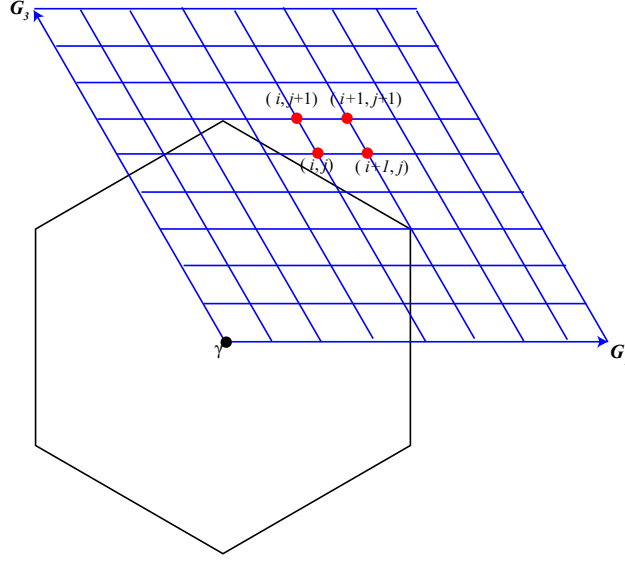


FIG. S4: A schematic plot of the Brillouin Zone formed with \mathbf{G}_1 and \mathbf{G}_3 . We discretized this Brillouin Zone to calculate the Chern number of the moiré bands.

where the Fourier components $V(\mathbf{G}' - \mathbf{G})$ and $\tilde{\mathbf{A}}(\mathbf{G}' - \mathbf{G})$ are obtained straightforwardly according to Eq. (1) and Eq. (S12), while $\tilde{A}^2(\mathbf{G}' - \mathbf{G}) = \frac{1}{S} \int d\mathbf{r} [\tilde{A}_x^2(\mathbf{r}) + \tilde{A}_y^2(\mathbf{r})] e^{-i\mathbf{G} \cdot \mathbf{r}}$. Specifically, we can obtain

$$\langle \mathbf{k} + \mathbf{G}' | \mathcal{H}_V | \mathbf{k} + \mathbf{G} \rangle = V_0 e^{i\phi} \sum_{j=1,3,5} \delta_{\mathbf{G}' - \mathbf{G}, \mathbf{G}_j} + V_0 e^{-i\phi} \sum_{j=2,4,6} \delta_{\mathbf{G}' - \mathbf{G}, \mathbf{G}_j}; \quad (\text{S84})$$

$$\begin{aligned} \langle \mathbf{k} + \mathbf{G}' | \mathcal{H}_{A \cdot \hat{\mathbf{p}}}(\mathbf{r}) | \mathbf{k} + \mathbf{G} \rangle &= \frac{\sqrt{3}\tau\gamma}{4i} (-\delta_{\mathbf{G}' - \mathbf{G}, \mathbf{G}_3} - \delta_{\mathbf{G}' - \mathbf{G}, \mathbf{G}_2} + \delta_{\mathbf{G}' - \mathbf{G}, \mathbf{G}_5} + \delta_{\mathbf{G}' - \mathbf{G}, \mathbf{G}_6})(\mathbf{k} + \mathbf{G})_x \\ &+ \frac{\tau\gamma}{4i} (2\delta_{\mathbf{G}' - \mathbf{G}, \mathbf{G}_1} - 2\delta_{\mathbf{G}' - \mathbf{G}, \mathbf{G}_4} - \delta_{\mathbf{G}' - \mathbf{G}, \mathbf{G}_3} + \delta_{\mathbf{G}' - \mathbf{G}, \mathbf{G}_6} - \delta_{\mathbf{G}' - \mathbf{G}, \mathbf{G}_5} + \delta_{\mathbf{G}' - \mathbf{G}, \mathbf{G}_2})(\mathbf{k} + \mathbf{G})_y; \end{aligned} \quad (\text{S85})$$

$$\begin{aligned} \langle \mathbf{k} + \mathbf{G}' | \mathcal{H}_{A^2} | \mathbf{k} + \mathbf{G} \rangle &= -\frac{\hbar^2}{2m^* L_M^2} \frac{\Phi^2}{\Phi_0^2} \left\{ \frac{3}{2} \delta_{\mathbf{G}, \mathbf{G}'} - \frac{1}{4} \sum_{\pm} (\delta_{\mathbf{G} - \mathbf{G}', \pm 2\mathbf{G}_1} + \delta_{\mathbf{G} - \mathbf{G}', \pm 2\mathbf{G}_2} + \delta_{\mathbf{G} - \mathbf{G}', \pm 2\mathbf{G}_3}) \right. \\ &\left. - \frac{1}{4} \sum_{\pm} (\delta_{\mathbf{G} - \mathbf{G}', \pm (\mathbf{G}_1 + \mathbf{G}_2)} - \delta_{\mathbf{G} - \mathbf{G}', \pm (\mathbf{G}_1 - \mathbf{G}_2)} + \delta_{\mathbf{G} - \mathbf{G}', \pm (\mathbf{G}_2 + \mathbf{G}_3)} - \delta_{\mathbf{G} - \mathbf{G}', \pm (\mathbf{G}_2 - \mathbf{G}_3)} - \delta_{\mathbf{G} - \mathbf{G}', \pm (\mathbf{G}_1 + \mathbf{G}_3)} + \delta_{\mathbf{G} - \mathbf{G}', \pm (\mathbf{G}_1 - \mathbf{G}_3)}) \right\}. \end{aligned} \quad (\text{S86})$$

Using above relations, we can obtain the matrix representation of $\hat{H}_{\mathbf{k}}(\mathbf{G}', \mathbf{G})$ with $\mathbf{G} = m\mathbf{G}_2 + n\mathbf{G}_3$. The moiré bands are calculated by diagonalizing $\hat{H}_{\mathbf{k}}(\mathbf{G}', \mathbf{G})$ numerically with a momentum cut-off of $-N \leq m, n \leq N$.

B. The Chern number of moiré bands

In the Fig.2 of main text, the Chern numbers of moiré bands were evaluated with various of phase ϕ and pseudo-magnetic field strength. To make the calculation more efficient, we used the method proposed in Ref. [69] to evaluate the Chern number, where the Brillouin zone is discretized. To be convenient, as shown in Fig. S4, we discretized the Brillouin zone formed with reciprocal lattice vector \mathbf{G}_1 and \mathbf{G}_3 , where the \mathbf{k} is spanned as discretized \mathbf{k} -points $\mathbf{k}_{i,j} = \frac{i}{N_t} \mathbf{G}_1 + \frac{j}{N_t} \mathbf{G}_3$. The Chern number of n -th band is given by

$$C = \sum_{i=1}^{N_t-1} \sum_{j=1}^{N_t-1} \ln[U_n(\mathbf{k}_{i,j}, \mathbf{k}_{i+1,j}) U_n(\mathbf{k}_{i+1,j}, \mathbf{k}_{i+1,j+1}) U_n(\mathbf{k}_{i+1,j+1}, \mathbf{k}_{i,j+1}) U_n(\mathbf{k}_{i,j+1}, \mathbf{k}_{i,j})], \quad (\text{S88})$$

where $U_n(\mathbf{k}_{i,j}, \mathbf{k}_{i',j'}) = \langle \psi_n(\mathbf{k}_{i,j}) | \psi_n(\mathbf{k}_{i',j'}) \rangle / |\langle \psi_n(\mathbf{k}_{i,j}) | \psi_n(\mathbf{k}_{i',j'}) \rangle|$ and $\psi_n(\mathbf{k}_{i,j})$ denote the eigen wavefunction obtained by diagonalizing the moiré Hamiltonian at momentum $\mathbf{k} = \mathbf{k}_{i,j}$. In the calculation, we took $N_t = 21$.

C. Hartree-Fock mean-field calculations

In the main text, we have presented the numerical results of Hartree-Fock mean-field calculations. In this section, we sketch the essential formalisms and processes to evaluate the energies of the SVP state and IVC states numerically. Here we consider a more general case, where the full mean-field Hamiltonian is given in Eq. (S54). As discussed, the order parameter is $\Delta(\mathbf{k}) = 1/2(1 + \tau_z)$ for the SVP state. The energy for the SVP state can thus be straightforwardly obtained as

$$E_{SVP} = \sum_{\mathbf{k}} \xi_+(\mathbf{k}) + \frac{V_0}{2N} \sum_{\mathbf{G}} v_{\mathbf{G}} \left| \sum_{\mathbf{k}'} \Lambda^+(\mathbf{k}' + \mathbf{G}, \mathbf{k}') \right|^2 - \frac{V_0}{2N} \sum_{\mathbf{k}, \mathbf{k}', \mathbf{G}} v_{\mathbf{k}' - \mathbf{k} + \mathbf{G}} |\Lambda^+(\mathbf{k}' + \mathbf{G}, \mathbf{k})|^2. \quad (\text{S89})$$

For the IVC state, by using the IVC order parameter given in Eq. (S71), we can obtain a similar mean-field Hamiltonian $H(\mathbf{k})$ as Eq. (S64) with

$$h_0(\mathbf{k}) = \frac{1}{2}(\xi_+(\mathbf{k}) + \xi_-(\mathbf{k})) + \frac{V_0}{2} \sum_{\mathbf{G}} \text{tr}[\Delta^H(\mathbf{G})](\Lambda^+(\mathbf{k} - \mathbf{G}, \mathbf{k}) + \Lambda^-(\mathbf{k} - \mathbf{G}, \mathbf{k})) - \frac{V_0}{2} \sum_{\mathbf{G}} (\Delta_{++}^F(\mathbf{k}, \mathbf{G}) + \Delta_{--}^F(\mathbf{k}, \mathbf{G})) \quad (\text{S90})$$

$$h_1(\mathbf{k}) = \frac{1}{2}(\xi_+(\mathbf{k}) - \xi_-(\mathbf{k})) + \frac{V_0}{2} \sum_{\mathbf{G}} \text{tr}[\Delta^H(\mathbf{G})](\Lambda^+(\mathbf{k} - \mathbf{G}, \mathbf{k}) - \Lambda^-(\mathbf{k} - \mathbf{G}, \mathbf{k})) - \frac{V_0}{2} \sum_{\mathbf{G}} (\Delta_{++}^F(\mathbf{k}, \mathbf{G}) - \Delta_{--}^F(\mathbf{k}, \mathbf{G})) \quad (\text{S91})$$

$$h_2(\mathbf{k}) = -V_0 \sum_{\mathbf{G}} \Delta_{+-}^F(\mathbf{k}, \mathbf{G}). \quad (\text{S92})$$

Here, the Hartree order parameter is given by

$$\Delta^H(\mathbf{G}) = \frac{v_{\mathbf{G}}}{N} \sum_{\mathbf{k}'} \begin{pmatrix} \Lambda^+(\mathbf{k}' + \mathbf{G}, \mathbf{k}') \sin^2 \frac{\theta_{\mathbf{k}'}}{2} & 0 \\ 0 & \Lambda^-(\mathbf{k}' + \mathbf{G}, \mathbf{k}') \cos^2 \frac{\theta_{\mathbf{k}'}}{2} \end{pmatrix} \quad (\text{S93})$$

and Fock order parameter is given by

$$\Delta^F(\mathbf{k}, \mathbf{G}) = \frac{1}{N} \sum_{\mathbf{k}'} v_{\mathbf{k}' - \mathbf{k} + \mathbf{G}} \begin{pmatrix} |\Lambda^+(\mathbf{k}' + \mathbf{G}, \mathbf{k})|^2 \sin^2 \frac{\theta_{\mathbf{k}'}}{2} & \frac{1}{2} \Lambda^+(\mathbf{k}' + \mathbf{G}, \mathbf{k}) \Lambda^-(\mathbf{k} - \mathbf{G}, \mathbf{k}') \sin \theta_{\mathbf{k}'} e^{i\varphi_{\mathbf{k}'}} \\ \frac{1}{2} \Lambda^-(\mathbf{k}' + \mathbf{G}, \mathbf{k}) \Lambda^+(\mathbf{k} - \mathbf{G}, \mathbf{k}') \sin \theta_{\mathbf{k}'} e^{-i\varphi_{\mathbf{k}'}} & |\Lambda^-(\mathbf{k}' + \mathbf{G}, \mathbf{k})|^2 \cos^2 \frac{\theta_{\mathbf{k}'}}{2} \end{pmatrix}. \quad (\text{S94})$$

The self-consistent equation reads

$$\cos \theta_{\mathbf{k}} = \frac{h_1(\mathbf{k})}{\sqrt{h_1^2(\mathbf{k}) + |h_2(\mathbf{k})|^2}}, \tan \varphi_{\mathbf{k}} = \frac{\text{Im}(h_2(\mathbf{k}))}{\text{Re}(h_2(\mathbf{k}))} \quad (\text{S95})$$

This self-consistent equation is solved iteratively. Specifically, we chose discrete \mathbf{k} points with $N \times N$ grid in the Brillouin Zone and set some initial values for $\theta_{\mathbf{k}}$ and $\varphi_{\mathbf{k}}$ with $\theta_{\mathbf{k}} = \pi - \theta_{-\mathbf{k}}$ and $\varphi_{\mathbf{k}} = \varphi_{-\mathbf{k}}$. In the Fig. 3 of main text, we set $N = 11$. Then we can evaluate $\theta_{\mathbf{k}}$ and $\varphi_{\mathbf{k}}$ with Eq. (S95). This can be done iteratively until the difference $\sum_{\mathbf{k}} |\theta_{\mathbf{k}}^{m+1} - \theta_{\mathbf{k}}^m|$ is smaller than a critical value such as 10^{-3} , where m labels the m -th iterative step.

After adding the potential term back, the total energy for the IVC state is obtained as

$$E_{IVC} = \sum_{\mathbf{k}} E_-(\mathbf{k}) - \frac{NV_0}{2} \sum_{\mathbf{G}} \frac{\text{tr}[\Delta^H(\mathbf{G})] \text{tr}[\Delta^H(-\mathbf{G})]}{v_{\mathbf{G}}} + \frac{V_0}{2N} \sum_{\mathbf{k}, \mathbf{k}', \mathbf{G}} v_{\mathbf{k}' - \mathbf{k} + \mathbf{G}} \text{tr}[\Lambda(\mathbf{k}' + \mathbf{G}, \mathbf{k}) \Delta(\mathbf{k}') \Lambda(\mathbf{k} - \mathbf{G}, \mathbf{k}') \Delta(\mathbf{k})]. \quad (\text{S96})$$

Note we need to further subtract a large density-like Hartree term from $\Delta^H(\mathbf{G} = 0)$, i.e., $E^H(\mathbf{G} = 0) = \frac{NV_0}{2} v_{\mathbf{G}=0}$, which does not affect the order but gives a large charge background and should be canceled with positive ion background. In other words, the total energy for the SVP state and IVC state are $\tilde{E}_{SVP} = E_{SVP} - E^H(\mathbf{G} = 0)$ and $\tilde{E}_{IVC} = E_{IVC} - E^H(\mathbf{G} = 0)$. The gap of the SVP states are defined as $\Delta_{SVP} = \min[\tilde{E}_{SVP,-}(\mathbf{k})] - \max[\tilde{E}_{SVP,+}(\mathbf{k})]$ and $\tilde{E}_{SVP,\tau}(\mathbf{k})$ represents the mean-field energy dispersion of the SVP state at momentum \mathbf{k} .

V. EFFECTIVE TIGHT-BINDING MODEL CALCULATION WITH LATTICE RELAXATION FOR MOIRÉ HETEROBILAYER TMDs

A. Lattice relaxation in moiré TMDs

Let us first illustrate the underlying mechanism of the lattice relaxation in moiré bilayer transition metal dichalcogenides (TMDs). As shown in Fig. S5(a), the lattice structure of a moiré bilayer TMD locally resembles the regular stacking, such as MX', MM' and XX' regions. Here, the M, X respectively denotes the transition metal atom and chalcogenide atom. To simplify the discussion, we can focus on the MX' and XX' stacking which change the adhesion energy most prominently. Specifically, at the MX' stacking region, the M and X' atoms are aligned with each other. In this case, the attraction between the transition metal atoms and chalcogenide atoms will locally lower the adhesion energy between the two layers. The MX' stacking configuration thus has the lowest energy as shown in the bottom right panel of Fig. S5(a), and actually corresponds to the stacking configuration of bulk 2H-structure TMDs. On the contrary, at the XX' stacking regions, the X and X' atoms are aligned with each other. Due to the repulsion between the chalcogenide atoms, the adhesion energy would be locally increased. Consequently, to save the adhesion energy [38], the heterobilayer TMDs lattice will relax itself to enlarge the MX'-stacking area and reduce the XX'-stacking area. If the intra-layer elastic energy caused by lattice relaxation can be compensated by lowering adhesion energy, the lattice relaxation will be energy favored. Indeed, lattice relaxation and even lattice reconstructions are commonly observed in various moiré materials [41–43].

The lattice relaxation can be characterized by the displacement vectors of atoms positions between the relaxed and unrelaxed lattice. Let us first look at the in-plane displacement vectors, which we denote as $\mathbf{u}^{(l)}(\mathbf{r})$. The layer index $l = 1$ for the WSe₂ layer, and $l = 2$ for the MoTe₂ layer. The lattice deformation is expected to keep the original superlattice period and respects the C_3 symmetry. As a result, we can express the in-plane displacement $\mathbf{u}^{(l)}(\mathbf{r})$ with the Fourier components $\mathbf{u}_{\mathbf{q}}^{(l)}$ as

$$\mathbf{u}^{(l)}(\mathbf{r}) = \sum_{\mathbf{q}} \mathbf{u}_{\mathbf{q}}^{(l)} e^{i\mathbf{q} \cdot \mathbf{r}}, \quad (\text{S97})$$

with $\mathbf{q} = m\mathbf{G}_1 + n\mathbf{G}_3$ with $\mathbf{G}_j = \frac{4\pi}{\sqrt{3}L_M}(\sin \frac{(j-1)\pi}{3}, \cos \frac{(j-1)\pi}{3})$. Note that in this section, we rotate the coordinate convention by ninety degree compared to the main text for the sake of convenience. For simplicity, we only keep the leading-order contributions from $\mathbf{u}_{\mathbf{q}}^{(l)}$ with $|\mathbf{q}| = G$, where $G = |\mathbf{G}_j| = \sqrt{3}\kappa$. To be more specific, we will also use $\mathbf{u}_{m,n}^{(l)}$ to label $\mathbf{u}_{\mathbf{q}}^{(l)}$ sometimes. Note that $\mathbf{u}_{0,0}^{(l)}$ is forced to vanish by the C_3 symmetry. Thus, we consider the Fourier components from six \mathbf{q} points in total. The point group symmetry requires $\mathbf{u}_{\hat{g}\mathbf{q}}^{(l)} = \hat{g}\mathbf{u}_{\mathbf{q}}^{(l)}$. Moreover, the displacement $\mathbf{u}^{(l)}(\mathbf{r})$ should be real, which requires $\mathbf{u}_{-\mathbf{q}}^{(l)} = \mathbf{u}_{\mathbf{q}}^{(l)*}$. Therefore, there is only one independent $\mathbf{u}_{\mathbf{q}}^{(l)}$ for each layer, and we will use the $\mathbf{u}_{1,0}^{(l)}$ component. As we will discuss later, the in-plane displacement can be chosen according to the strength of build-in strain found by the DFT results [43, 49].

Apart from in-plane relaxation, the heterobilayers will also exhibit out-of-plane corrugation. The interlayer distance which minimizes the adhesion energy can be inferred from the bottom right panel of Fig. S5(a). The lattice tends to exhibit a minimum inter-layer spacing at the MX'-stacking regions due to the attraction between the transition metal atoms and chalcogenide atoms, while has a maximum inter-layer distance at the XX'-stacking region, which gives rise to the corrugation effect.

To capture this corrugation effect, we define the out-of-plane displacement of the two layers as $h^{(l)}(\mathbf{r})$. The inter-layer spacing can thus be written as $d(\mathbf{r}) = d_0 + \Delta h(\mathbf{r})$ with $\Delta h(\mathbf{r}) = h^{(2)}(\mathbf{r}) - h^{(1)}(\mathbf{r})$, where d_0 is the average spacing between the two layers. The Fourier components $h_{\mathbf{q}}^{(l)}$ for the out-of-plane corrugation is written as

$$h^{(l)}(\mathbf{r}) = \sum_{\mathbf{q}} h_{\mathbf{q}}^{(l)} e^{i\mathbf{q} \cdot \mathbf{r}}. \quad (\text{S98})$$

Still, only the leading-order contributions from $h_{\mathbf{q}}^{(l)}$ with $|\mathbf{q}| = G$ is kept. The point group symmetry gives $h_{\hat{g}\mathbf{q}}^{(l)} = h_{\mathbf{q}}^{(l)}$, and a real displacement $h^{(l)}(\mathbf{r})$ requires $h_{-\mathbf{q}}^{(l)} = h_{\mathbf{q}}^{(l)*}$. To show the interlayer distance given by Eq. S98 in moiré heterobilayer MoTe₂/WSe₂, we plotted the inter-layer distance as shown in Fig. S5(c), where we set $\Delta h_{1,0} = -(2.4 + 6.2i) \times 10^{-3}$ nm, $d_0 = 0.7$ nm that fit the DFT results [43, 49]. As expected, the interlayer spacing is maximum at XX' stacking region and minimum at the MX'-stacking region.

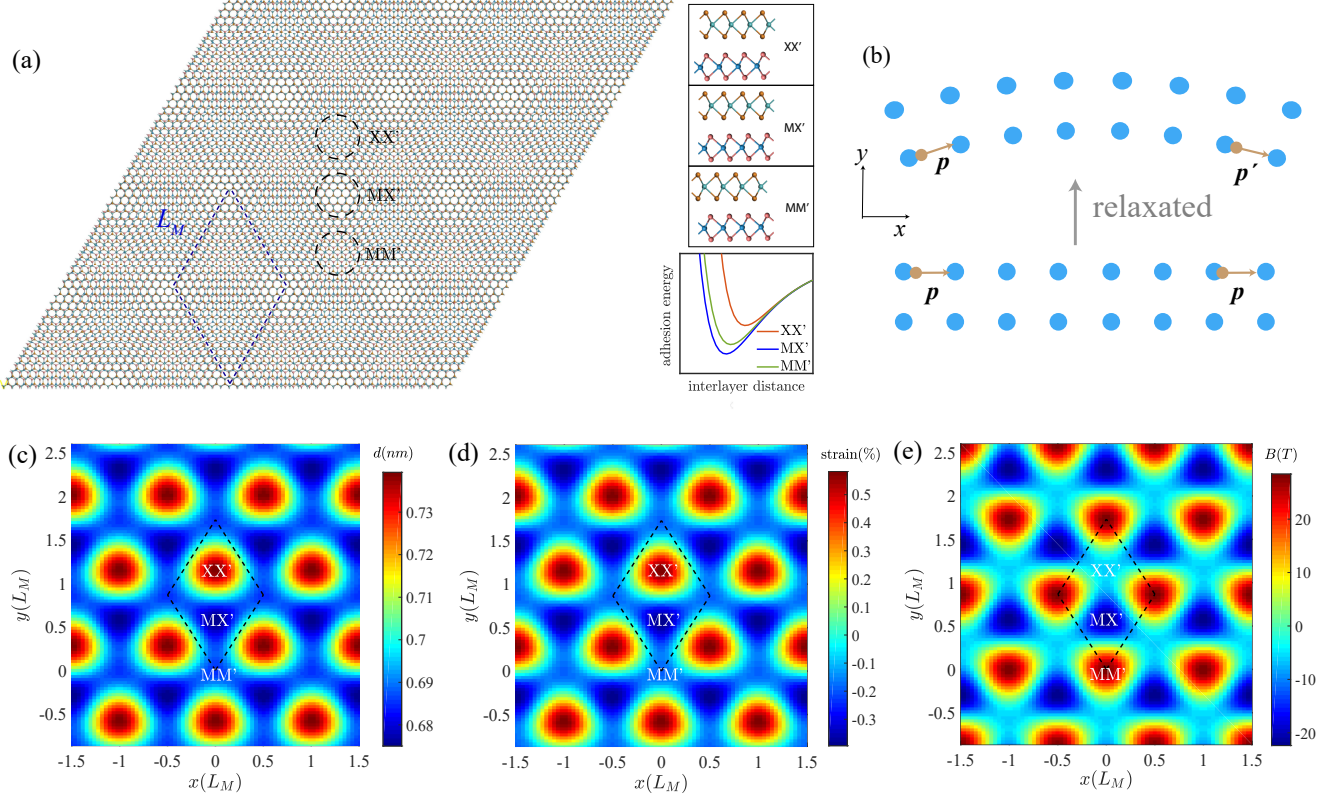


FIG. S5: (a) Moiré supercell marked with blue dashed line, and the local MM', MX', XX' stacking configurations highlighted with black dashed circles of heterobilayer MoTe₂/WSe₂ in the zero twist angle limit. The side views of different stacking areas are magnified in the top right panel. The adhesion energy with respect to interlayer distance for the three stacking configurations is schematically shown in the bottom right panel [38]. (b) schematically shows a uniform lattice and a lattice with some in-plane distortions. The \mathbf{p} represents the momentum with a direction along the arrow. (c) Inter-layer distance which shows strong out-of-plane corrugation. (d) In-plane strain field (trace of the strain tensor) in the MoTe₂ layer. (e) Pseudo-magnetic field in the MoTe₂ layer. We have adopted the following parameters in accordance with the DFT results [43, 49]: $\mathbf{u}_{1,0}^{(2)} = (0, -0.6 + 0.2i) \times 10^{-3}$ nm, $\Delta h_{1,0} = -(2.4 + 6.2i) \times 10^{-3}$ nm, $d_0 = 0.7$ nm and $\beta = 2$. Note that we set the x -component of $\mathbf{u}_{1,0}$ to be zero due to the mirror symmetry M_x in the untwisted heterobilayer TMDs.

B. Pseudomagnetic fields emerged from the atomic lattice relaxation in moiré TMDs

After discussing the lattice relaxation in moiré TMDs, we next introduce how the pseudomagnetic fields can be generated by such periodic lattice displacement. To give an intuitive physical picture why the pseudomagnetic fields can arise from lattice relaxation in general, we depicted Fig. S5 which shows a uniform lattice and a distorted lattice after the lattice relaxation. Phenomenologically, the momentum of an electron moves along the lattice is preserved in the uniform case, while the momentum of an electron moves along a distorted lattice has to be gradually changed (see Fig. S5(b)). The scenario in the distorted lattice mimics an electron circulating an out-of-plane magnetic fields by the Lorentz force classically. From this simple picture, it is understandable that the lattice relaxation could give rise to the effects of pseudo-magnetic fields.

It was known that the pseudo-magnetic fields from the lattice relaxation can be directly obtained from the strain tensor, which is defined as the spatial gradients of the displacement field [52, 67, 70]

$$u_{ij}^{(l)} = \frac{1}{2}(\partial_i u_j^{(l)} + \partial_j u_i^{(l)} + \partial_i h^{(l)} \partial_j h^{(l)}). \quad (\text{S99})$$

The in-plane displacement u_i^l and out-of-plan displacement h^l are defined in Eq. (S97) and Eq. (S98), respectively. The last term represents the in-plane strain induced by the out-of-plane corrugation, which we find to be a second-order effect and will be neglected in the following discussion for simplicity. Then, the strain tensor can be expressed with

the Fourier components as

$$u_{ij}^{(l)}(\mathbf{r}) = \frac{i}{2} \sum_{\mathbf{q}} (q_i u_{\mathbf{q},j}^{(l)} + q_j u_{\mathbf{q},i}^{(l)}) e^{i\mathbf{q} \cdot \mathbf{r}}. \quad (\text{S100})$$

To be specific, we consider an in-plane displacement field with Fourier component $\mathbf{u}_{1,0}^{(2)} = (0, -0.6 + 0.2i) \times 10^{-3}$ nm, and the calculated in-plane strain field (trace of the strain tensor) of the MoTe₂ layer using Eq. (S100) is plotted in Fig. S5(d). Note that the Fourier component of in-plane displacement is set to give rise to roughly 0.5% built-in strain strength revealed by previous DFT calculations for moiré TMDs [43, 49]. As shown in Fig. S5(d), the strain at the MX'-stacking region is compressive, while the strain at XX'-stacking region is tensile. As the MoTe₂ layer possesses larger lattice constant than WSe₂ layer, such relaxation could effectively increase the MX'-stacking region and reduce the XX'-stacking region to save energy.

As we presented in the main text, the strain tensor will induce an effective gauge field \mathbf{A} . We thus can map out pseudomagnetic fields from lattice relaxation as $\mathbf{B} = \nabla \times \mathbf{A}$. Specifically, the effective gauge field from the strain is given by

$$\mathbf{A}^{(l)} = \frac{\sqrt{3}\beta\hbar}{2ea} (u_{xx}^{(l)} - u_{yy}^{(l)}, -2u_{xy}^{(l)}) = \frac{\sqrt{3}\beta\Phi_0}{4\pi a} i \sum_{\mathbf{q}} (q_x u_{\mathbf{q},x}^{(l)} - q_y u_{\mathbf{q},y}^{(l)}, -q_x u_{\mathbf{q},y}^{(l)} - q_y u_{\mathbf{q},x}^{(l)}) e^{i\mathbf{q} \cdot \mathbf{r}}, \quad (\text{S101})$$

where the strain tensor form from Eq. (S100) is inserted, the value of β depends on the specific material or model, and $\Phi_0 = \frac{h}{e}$ is the flux quantum. This results in an out-of-plane pseudomagnetic field [52, 70]

$$B_z^{(l)} = \partial_x A_y^{(l)} - \partial_y A_x^{(l)} = \frac{\sqrt{3}\beta\Phi_0}{4\pi a} \sum_{\mathbf{q}} [(q_x^2 - q_y^2) u_{\mathbf{q},y}^{(l)} + 2q_x q_y u_{\mathbf{q},x}^{(l)}] e^{i\mathbf{q} \cdot \mathbf{r}}. \quad (\text{S102})$$

We plot the distribution of the pseudomagnetic field in the MoTe₂ layer in Fig. S5(e) with $\beta = 2$. A periodic pseudomagnetic field can be achieved in the presence of the lattice relaxation, which is expected for moiré TMD materials [38]. Note that it is mainly the spatial gradient of strain fields rather than the strength of strain only determines the magnitude of pseudomagnetic fields. For example, the XX' stacking region in Fig. S5(d) displays a sizable tensile strain ($\sim 0.5\%$), while the corresponding pseudomagnetic field is small (see Fig. S5(e)). In contrast, the strain configuration given in Fig. S5(d) exhibits largest spatial gradients near MM' regions, which results in largest pseudomagnetic fields (see Fig. S5(e)).

C. Effective strained tight-binding model for MoTe₂/WSe₂ heterobilayers

To calculate the band structure and study its topology in the presence of lattice relaxation, we further write a tight-binding model for the MoTe₂ monolayer, and treat the effect of the WSe₂ layer as a moiré potential. The moiré supercell of MoTe₂/WSe₂ heterobilayers in zero twist angle limit contains 13×13 MoTe₂ unit cells and 14×14 WSe₂ unit cells. We will construct the tight-binding Hamiltonian using the six d-orbitals $\{|d_{z^2,s}\rangle, |d_{xy,s}\rangle, |d_{x^2-y^2,s}\rangle\}$ with $s = \uparrow / \downarrow$ from the transition metal atoms [68]. As there are 13×13 Mo atoms in each moiré unit cell (see Fig. S6(a)), the dimension of our tight-binding Hamiltonian is $13 \times 13 \times 6 = 1014$.

First of all, the unstrained tight-binding Hamiltonian up to nearest-neighbor hopping is written as [68]

$$H_0 = \sum_{\mathbf{k}, \mathbf{R}_i} \sum_{\delta_j} c_{\mathbf{k}, \mathbf{R}_i}^\dagger E_0(\delta_j) c_{\mathbf{k}, \mathbf{R}_i + \delta_j}, \quad (\text{S103})$$

where \mathbf{R}_i labels the positions of the 13×13 Mo atoms, $c_{\mathbf{k}, \mathbf{R}_i}^\dagger$ denotes the creation operator of the Bloch states with momentum \mathbf{k} (defined in moiré Brillouin zone), δ_j are the lattice vectors connecting the sites, and $E_0^{\alpha\alpha'}(\delta_j) = \langle \phi^\alpha(\mathbf{r}) | \hat{H} | \phi^{\alpha'}(\mathbf{r} - \delta_j) \rangle$ is the hopping integral. The on-site energy and the nearest-neighbor hopping term take the form:

$$E_0(\delta = 0) = \sigma_0 \otimes \begin{pmatrix} \epsilon_1 & 0 & 0 \\ 0 & \epsilon_2 & 0 \\ 0 & 0 & \epsilon_2 \end{pmatrix} - \mu I_{6 \times 6}, \quad (\text{S104})$$

$$E_0(\delta = \mathbf{a}'_1) = \sigma_0 \otimes \begin{pmatrix} t_0 & t_1 & t_2 \\ -t_1 & t_{11} & t_{12} \\ t_2 & -t_{12} & t_{22} \end{pmatrix}, \quad (\text{S105})$$

and the hopping terms along other directions can be determined by symmetry as:

$$E_0(\hat{g}\delta_j) = D(\hat{g})E_0(\delta_j)D^\dagger(\hat{g}), \quad (\text{S106})$$

where $D(\hat{g})$ is representation of the symmetry operation \hat{g} under the six-orbital basis.

The SOC term takes the form of

$$H_{SOC} = \sum_{\mathbf{k}, \mathbf{R}_i} c_{\mathbf{k}, \mathbf{R}_i}^\dagger \left(\frac{\lambda}{2} \sigma_z \otimes L_z \right) c_{\mathbf{k}, \mathbf{R}_i}, \quad (\text{S107})$$

where $L_z = \begin{pmatrix} 0 & 0 & 0 \\ 0 & 0 & -2i \\ 0 & 2i & 0 \end{pmatrix}$ is the z -component of the orbital angular momentum. It should be noted the coordinated convention here is rotated by 90° compared to the main text. In the following presentation, we fixed the coordinated convention to be the same as this tight-binding model.

Supplementary Table 1: Parameters for unstrained tight-binding Hamiltonian of monolayer MoTe₂ adapted from Refs.[68]. All parameters set in units of eV.

ϵ_1	ϵ_2	t_0	t_1	t_2	t_{11}	t_{12}	t_{22}	λ
0.605	1.972	-0.169	0.228	0.390	0.207	0.239	0.252	-0.107

As we mentioned, due to the moiré potential, the unit cell is extended as the moiré unit cell which contains 13×13 Mo atoms. The hopping terms are captured by the above tight-binding Hamiltonian. Next, let us add the moiré potential introduced by the WSe₂ layer and the effects from the periodic strain fields $\mathbf{u}(\mathbf{r})$ that contains the pseudomagnetic fields. To be consistent with the main text and reduce the number of parameters, we will focus on these effects on the valence band only, where the top moiré bands are originated from. In other words, the strain and moiré terms will be added in the $(|d_{xy,s}\rangle, |d_{x^2-y^2,s}\rangle)$ subspace. Note that such simplification neglect the physics from the inter-orbital mixing from the conduction and valence band, which is not the focus of this work and we will leave this as a future study.

Let us discuss how the tight-binding Hamiltonian is changed in the presence of the strain fields first. Due to the displacement of atoms, when the strain \mathbf{u} is present, the hopping terms between the atomic orbitals will be modified:

$$E_0(\delta_j) \rightarrow E_0(\delta_j) + E_s(\overleftrightarrow{\mathbf{u}}, \delta_j), \quad (\text{S108})$$

which gives an extra contribution to the Hamiltonian

$$H_s = \sum_{\mathbf{k}, \mathbf{R}_i} \sum_{\delta_j} c_{\mathbf{k}, \mathbf{R}_i}^\dagger E_s[\overleftrightarrow{\mathbf{u}}(\mathbf{R}_i), \delta_j] c_{\mathbf{k}, \mathbf{R}_i + \delta_j}. \quad (\text{S109})$$

Here, the spatial dependence of $\mathbf{u}(\mathbf{R}_i)$ in each moiré unit cell is obtained by submitting the positions of transition metal atoms into Eq. (S100), and as we will show, the strain tensor $\overleftrightarrow{\mathbf{u}}$ would be decomposed as $u_0 = u_{xx} + u_{yy}$ and $(u_1, u_2) = (u_{xx} - u_{yy}, -2u_{xy})$. The former transforms as a scalar, while the latter transforms as a vector, i.e., E -representation, under C_3 operation.

Based on the symmetry analysis[71, 72], to linear order of the strain tensor, the contribution to the on-site energy is

$$\begin{aligned} E_s(\overleftrightarrow{\mathbf{u}}, \delta_j = 0) &= \sigma_0 \otimes \left[(u_{xx} + u_{yy}) \begin{pmatrix} E_2^S & 0 \\ 0 & E_2^S \end{pmatrix} + 2u_{xy} \begin{pmatrix} 0 & h_2^S \\ h_2^S & 0 \end{pmatrix} \right. \\ &\quad \left. + (u_{xx} - u_{yy}) \begin{pmatrix} h_2^S & 0 \\ 0 & -h_2^S \end{pmatrix} \right], \end{aligned} \quad (\text{S110})$$

and the modification for the nearest-neighbor hopping term along \mathbf{a}'_1 direction is

$$E_s(\overleftarrow{\mathbf{u}}, \boldsymbol{\delta}_j = \mathbf{a}'_1) = \sigma_0 \otimes \left[(u_{xx} + u_{yy}) \begin{pmatrix} P_{11}^{(A_1)} & P_{12}^{(A_1)} \\ -P_{12}^{(A_1)} & P_{22}^{(A_1)} \end{pmatrix} + (u_{xx} - u_{yy}) \begin{pmatrix} P_{11}^{(E)} & P_{12}^{(E)} \\ -P_{12}^{(E)} & P_{22}^{(E)} \end{pmatrix} \right. \\ \left. + 2u_{xy} \begin{pmatrix} 0 & N_{12}^{(E)} \\ N_{12}^{(E)} & 0 \end{pmatrix} \right]. \quad (\text{S111})$$

The hopping terms along other directions can be obtained by symmetry [71, 72]

$$E_s(\overleftarrow{\mathbf{u}}, \hat{g}\boldsymbol{\delta}_j) = D(\hat{g})E_s(\hat{g}^{-1}\overleftarrow{\mathbf{u}}, \boldsymbol{\delta}_j)D^\dagger(\hat{g}). \quad (\text{S112})$$

Without loss of generality, we adopt the strained tight-binding parameters up to nearest-neighbor hopping terms for the monolayer TMD [71] estimated from first-principle calculations. Substituting the strain configuration given by Eq. S100 into Eqs. S110, S111 and S112, we can obtain how the hopping terms are modified under strain. Notice that a significant difference from previous works [71, 72] is that the strain tensor from Eq. S100 are not uniform but spatially dependent with moiré periodicity.

Supplementary Table 2: Strained tight-binding parameters up to nearest-neighbor hopping terms for monolayer TMD adapted from Refs.[71]. All parameters are set in units of eV.

E_2^S	h_2^S	$P_{11}^{(A_1)}$	$P_{12}^{(A_1)}$	$P_{22}^{(A_1)}$	$P_{11}^{(E)}$	$P_{12}^{(E)}$	$P_{22}^{(E)}$	$N_{12}^{(E)}$
-1.012	-0.220	-1.127	0.325	1.617	-0.966	-0.044	1.179	-0.776

Finally, we take into account the moiré potential introduced by the WSe₂ layer as $V(\mathbf{r}) = \sum_{\mathbf{q}} V_{\mathbf{q}} e^{i\mathbf{q} \cdot \mathbf{r}} = 2V_0 \sum_{j=1,3,5} \cos(\mathbf{G}_j \cdot \mathbf{r} + \phi)$ with $\mathbf{G}_j = \frac{4\pi}{\sqrt{3}L_M} (\sin \frac{(j-1)\pi}{3}, \cos \frac{(j-1)\pi}{3})$ which gives a spatial-dependent on-site energy $H_V = \sum_{\mathbf{k}, \mathbf{R}_i} c_{\mathbf{k}, \mathbf{R}_i}^\dagger V(\mathbf{R}_i) c_{\mathbf{k}, \mathbf{R}_i}$. Note that as we mentioned, to be consistent with the main text, the moiré potential is only added on the valence bands. To be specific, we adopted $V_0 = 10$ meV, $\phi = 0.3\pi$ in the following calculations.

Now the total moiré strained tight-binding Hamiltonian reads

$$H_t = \sum_{\mathbf{k}, \mathbf{R}_i} \sum_{\boldsymbol{\delta}_j} c_{\mathbf{k}, \mathbf{R}_i}^\dagger [E_0(\boldsymbol{\delta}_j) + E_s(\overleftarrow{\mathbf{u}}, \boldsymbol{\delta}_j)] e^{i\mathbf{k} \cdot \boldsymbol{\delta}_j} c_{\mathbf{k}, \mathbf{R}_i + \boldsymbol{\delta}_j} + H_{SOC} + H_V. \quad (\text{S113})$$

By numerically diagonalizing H_t , we can investigate how the moiré bands are modified under the periodic strain fields $\mathbf{u}(\mathbf{r})$ induced by lattice relaxation. The advantage of this tight-binding model description is that it directly maps out the effects of the atomic displacements induced by the lattice relaxation on the moiré bands, as we will see next.

D. Moiré band structures and band topology from the strained tight-binding Hamiltonian

In this section, we present the moiré band structures and a switch in band topology for MoTe₂/WSe₂ heterobilayer layer under lattice relaxation using the effective tight-binding model Eq. (S113). As we discussed, the strain tensor can be decomposed as the scalar part $u_0(\mathbf{r}) = u_{xx}(\mathbf{r}) + u_{yy}(\mathbf{r})$ and the vector part $(u_1(\mathbf{r}), u_2(\mathbf{r})) = (u_{xx}(\mathbf{r}) - u_{yy}(\mathbf{r}), -2u_{xy}(\mathbf{r}))$. As expected, we find the scalar part $u_0(\mathbf{r})$ is mainly to modify the onsite-energy and thus effectively shift the moiré potential, including the strength V_0 and the phase ϕ , while the vector part $(u_1(\mathbf{r}), u_2(\mathbf{r}))$ is to generate the pseudomagnetic fields that could drive a topological band inversion. As our main focus is the effects from strain $(u_1(\mathbf{r}), u_2(\mathbf{r}))$, we will fix the strength of the scalar part with the maximal u_0 within the moiré unit cell $\sim 0.5\%$, being comparable to the previous first principle calculation [43, 49].

To demonstrate the lattice relaxation could switch the topology of top moiré bands, we artificially tuned the strength of $u_{xx}(\mathbf{r}) - u_{yy}(\mathbf{r})$ and $u_{xy}(\mathbf{r})$, i.e., $(u_1(\mathbf{r}), u_2(\mathbf{r})) \mapsto \lambda(u_1(\mathbf{r}), u_2(\mathbf{r}))$ and change λ gradually. The results are summarized in Fig. S6. As $u_{xx}(\mathbf{r}) - u_{yy}(\mathbf{r})$ and $u_{xy}(\mathbf{r})$ exhibit similar strain strength, without loss of generality,

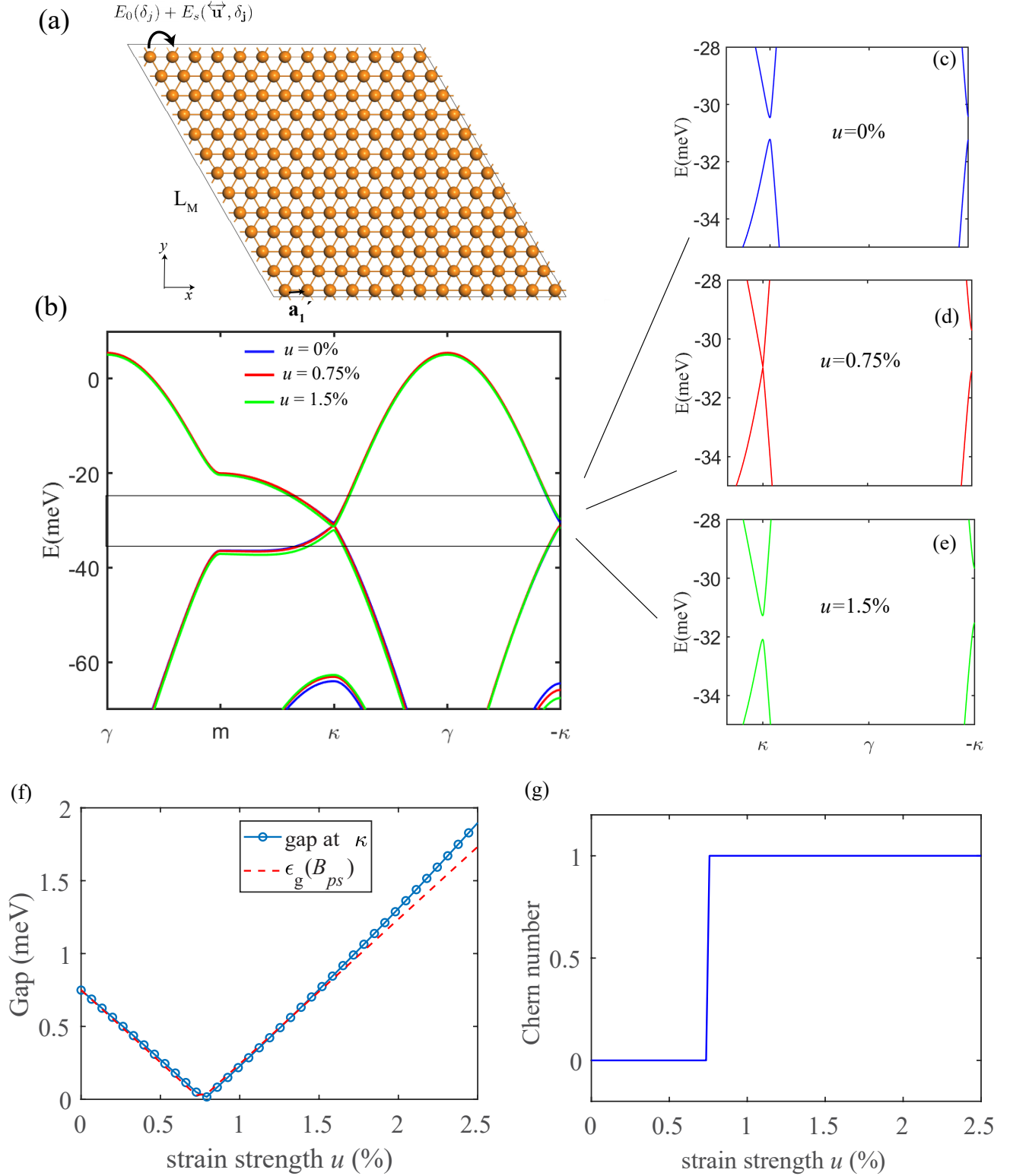


FIG. S6: (a) A schematic plot of 13×13 Mo atoms in each moiré unit cell, where the modified nearest-neighbor hopping under lattice relaxation, i.e., Eq. (S108), is highlighted. (b) shows the moiré band structures without strain (blue) and with strain strength $u = 0.75\%$ (red) and $u = 1.5\%$ (green). The strain strength u is defined as the maximal value of $u_{xy}(\mathbf{r})$ within the moiré unit cell. (c), (d), (e) are enlarged from (b) near $[-28, 35]$ meV, which clearly indicates a band inversion at κ valley when the strain strength exceeds 0.75%. (f) shows the separation between the first and the second moiré bands at κ valley, as a function of strain strength u . The red dashed line is plotted with $\epsilon_g(B_{ps}) \approx |\epsilon_g(0) - 0.05B_{ps}|$ (see Eq. S115), where B_{ps} denotes the magnitude of pseudomagnetic fields induced by the lattice relaxation. (g) shows the Chern number of the top moiré band as a function of strain strength u .

we will represent the strain strength with the maximal value of $u_{xy}(\mathbf{r})$ in within the moiré unit cell, and this value would be referred as the strain strength u in the following discussions.

Fig. S6(b) shows the moiré band structures with the strain strength $u = 0, 0.75\%, 1.5\%$ at K valley, which is compatible with the band structures obtained from the continuum model of main text. Here, we can distinguish the bands from the two different valleys ($\pm K$) as they exhibit opposite spin polarization. It can be seen that the energy change caused by the strain ($u_1(\mathbf{r}), u_2(\mathbf{r})$) ($\sim \text{meV}$) on the band structures is much smaller than the band width (tens of meV). However, being consistent with the main text, we find this small change is enough to drive a topological band inversion at moiré κ valley (see Fig. S6(c), (d) and (e)). The gap at κ and the Chern number of top moiré band as a function of the strain strength u is displayed in Fig. S6(f) and Fig. S6(g), respectively. It clearly shows that the top moiré band becomes topological after the gap is inverted by the strain. The topological gap, orders of one meV, is also consistent with the experiments [34]. The results from the strained tight-binding model that takes account of the atomic displacement induced by the lattice relaxation directly are thus in agreement with our results of main text

E. From tight-binding model to continuum model

To further demonstrate this consistency, let us estimate the gap according to the pseudomagnetic field generated by the strain configuration ($u_1(\mathbf{r}), u_2(\mathbf{r})$). As we mentioned in Eq. (S101), to know the pseudomagnetic field, we need to obtain the parameter β that characterizes how strong the strain couples with the electron's momentum. It can be obtained by comparing the energy dispersion of the strained tight-binding model and the effective continuum model Hamiltonian.

According to symmetry analysis, the continuum Hamiltonian near K valley under strain takes the form

$$H_{eff} = -\frac{\hbar^2 k^2}{2m^*} + f_0(u_{xx} + u_{yy}) + f_1 a[(u_{xx} - u_{yy})k_x - 2u_{xy}k_y]. \quad (\text{S114})$$

The values of the parameters can be determined by fitting the energy dispersion of the tight-binding model near K valley, which gives $m^* = 0.6357m_e$, $f_1 \approx 0.5826 \text{ eV}$. Note that the second term in Eq. (S114) is not relevant to our discussion and will be compensated by the chemical potential term. Comparing with the definition of the gauge field $\mathbf{A} = \frac{\sqrt{3}\beta\hbar}{2ea}(u_{xx} - u_{yy}, -2u_{xy})$, we find $\beta = \frac{2m^*a^2}{\sqrt{3}\hbar^2}f_1 = 0.72$.

After getting the value of β , we can obtain the pseudomagnetic field $B(\mathbf{r})$ from each strain configuration ($u_1(\mathbf{r}), u_2(\mathbf{r})$) according to Eq. (S101) and Eq. (S102). According to the main text, the magnitude of the pseudomagnetic field $B_{ps} = B(\mathbf{r} = 0)/3$ and the gap change ratio is 0.05 meV/T . The gap at the moiré κ valley is thus expected to be

$$\epsilon_g(B_{ps}) \approx |\epsilon_g(0) - 0.05B_{ps}|. \quad (\text{S115})$$

In this way, we estimated the gap at κ as a function of strain strength of $(u_{xx} - u_{yy}, u_{xy})$, as shown in Fig. S6(f) (red line). It clearly shows the gap directly calculated from the strained tight-binding model matches with the pseudomagnetic field picture of the main text.